Advancing excited-state properties of two-dimensional materials using a dielectric-dependent hybrid functional

Arghya Ghosh,[1] Subrata Jana,[2, *] Manoar Hossain,[3] Dimple Rani,[4] Szymon Śmiga,[2] and Prasanjit Samal[4]

[1]*Department of Physics, Indian Institute of Technology, Hyderabad, India*
[2]*Institute of Physics, Faculty of Physics, Astronomy and Informatics,*
Nicolaus Copernicus University in Toruń, ul. Grudziądzka 5, 87-100 Toruń, Poland
[3]*Paderborn Center for Parallel Computing, Paderborn University,*
Warburger Str. 100, 33098 Paderborn, Germany
[4]*School of Physical Sciences, National Institute of Science Education and Research,*
An OCC of Homi Bhabha National Institute, Bhubaneswar 752050, India

Predicting accurate band gaps and optical properties of lower-dimensional materials, including two-dimensional van der Waals (vdW) materials and their heterostructures, remains a challenge within density functional theory (DFT) due to their unique screening compared to their bulk counterparts. Additionally, accurate treatment of the dielectric response is crucial for developing and applying screened-exchange dielectric-dependent range-separated hybrid functionals (SE-DD-RSH) for vdW materials. In this work, we introduce a SE-DD-RSH functional to the 2D vdW materials like MoS_2, WS_2, hBN, black phosphorus (BP), and β-InSe. By accounting for in-plane and out-of-plane dielectric responses, our method achieves accuracy comparable to advanced many-body techniques like G_0W_0 and BSE@G_0W_0 at a lower computational cost. We demonstrate improved band gap predictions and optical absorption spectra for both bulk and layered structures, including some heterostructures like MoS_2/WS_2. This approach offers a practical and precise tool for exploring electronic and optical phenomena in 2D materials, paving the way for efficient computational studies of layered systems.

I. INTRODUCTION

Two-dimensional (2D) van der Waals (vdW) materials, sparked by graphene's discovery [1], have transformed materials science over the past two decades and rapidly expanded, uncovering new prospects for both fundamental science and technological applications [2–9]. These atomically thin layers, such as transition metal dichalcogenides (TMDCs), hexagonal boron nitride (hBN), black phosphorus (BP), and transition metal monochalcogenides (TMMCs) have garnered significant attention due to their unique electronic, optical, and mechanical properties [10–17]. These materials exhibit some interesting phenomena such as bandgap tunability, spin-valve effects, proximity-induced effects, surface and interface effects, optoelectronic properties, and superconductivity [18–23], making them ideal candidates for next-generation electronic and optoelectronic devices.

The remarkable properties of 2D vdW materials have spurred extensive theoretical investigations to understand and predict their behavior. Kohn-Sham (KS) density functional theory (DFT) has emerged as the state-of-the-art approach to study their fundamental characteristics [24–28]. However, the accuracy of DFT calculations strongly depends on the choice of the exchange and correlation (XC) [29–37]. While semilocal XC approximations offer reliable predictions for ground-state properties [38–45], they often fail to capture excited-state phenomena such as bandgaps and optical absorption spec-

tra [46, 47]. To address these limitations, it is necessary to go beyond semilocal approximations and incorporate Fock non-local exchange [48–53]. Within KS-DFT, this is achieved through hybrid density functionals, which provide reasonably accurate results for extended solids. While hybrid functionals improve accuracy for bulk materials, their fixed mixing parameters often struggle to describe the altered screening in lower-dimensional 2D vdW materials aterials [29, 54], necessitating more tailored approaches.

To overcome these challenges, many-body perturbation theory (MBPT) [55–58] has emerged as a powerful alternative for accurately predicting the quasi-particle band structure and optical properties of 2D vdW materials. The Green's function-based GW approximation [58–69] and the Bethe-Salpeter equation (BSE) [70–78] offer more accurate descriptions of excited-state phenomena by incorporating dynamic screening and electron-hole interactions. While GW captures the essential dynamic screening effects necessary for accurate bandgap calculations, its high computational cost remains a significant challenge. Among the different GW variants, the non-self-consistent single-shot G_0W_0 method is often preferred for its balance between accuracy and computational efficiency. However, despite this advantage, G_0W_0 remains sensitive to the choice of the initial DFT starting point [69, 79–81]. To mitigate this limitation, dielectric-dependent hybrid functionals (DDHs) have gained attention as computationally efficient alternatives for predicting band gaps in 2D vdW solids. By replacing the fixed Fock mixing parameter with a material-specific dielectric constant [72, 74, 82–85], DDHs bridge the gap between hybrid functionals and MBPT methods. However, de-

termining the optimal mixing and range-separation parameters remains a key challenge, particularly for 2D systems, where conventional approaches used for 3D material [80, 81, 83–90], may not be directly applicable [72, 74, 82].

In this study, we employ screened-exchange dielectric-dependent range-separated hybrid (SE-DD-RSH) functional to systematic investigation of the bandgaps and optical properties of 2D Van der Waals (vdW) materials. The proposed screened DDH functional achieves accuracy comparable to the highly demanding and computationally intensive G_0W_0 and BSE@G_0W_0 methods, offering a more efficient alternative for predicting electronic and optical properties.

The paper is structured as follows: Section II outlines the theoretical background of both existing and newly developed screened-exchange dielectric-dependent range-separated hybrid functionals. Section III presents a benchmark study and explores applications of the screened DDH functional for several prototypical vdW materials. Finally, Section IV summarizes our findings and key conclusions.

II. SCREENED RANGE-SEPARATED HYBRID FOR LAYERS

A. Overview of screened range-separated hybrid

The range-separated hybrid (RSH) density functional formalism introduces a refined treatment of exchange interactions by employing the Coulomb-attenuated method (CAM) to partition the two-electron operator [74, 83, 84, 86, 87, 89–100],

$$\frac{1}{r_{12}} = \frac{\alpha + (\gamma - \alpha)\,\mathrm{erf}(\mu r_{12})}{r_{12}} + \frac{1 - [\alpha + (\gamma - \alpha)\,\mathrm{erf}(\mu r_{12})]}{r_{12}}.$$

(1)

where $\frac{1}{r_{12}} = \frac{1}{|\mathbf{r}_1 - \mathbf{r}_2|}$ represents the Coulomb interaction between two electrons, α and γ, and μ are key parameters that define the separation between short- and long-range exchange interactions. By incorporating the Perdew-Burke-Ernzerhof (PBE) [101] XC and Fock exchange into Eq. 1, the exchange-correlation energy can be expressed as a sum of short-range (sr) and long-range (lr) components:

$$E_{xc}^{RSH}(\alpha, \gamma; \mu) = (1 - \alpha)E_x^{\mathrm{PBE\text{-}sr},\mu} + \alpha E_x^{\mathrm{Fock\text{-}sr},\mu}$$
$$+ (1 - \gamma)E_x^{\mathrm{PBE\text{-}lr},\mu} + \gamma E_x^{\mathrm{Fock\text{-}lr},\mu} + E_c^{\mathrm{PBE}}.$$

(2)

and the corresponding exchange-correlation potential is given by

$$\begin{aligned} V_{xc}^{RSH}(\mathbf{r}, \mathbf{r}', \alpha, \gamma; \mu) &= [\alpha + (\alpha - \gamma)\,\mathrm{erf}(\mu r)]\, V_x^{\mathrm{Fock}}(\mathbf{r}, \mathbf{r}') \\ &- (\alpha - \gamma)V_x^{\mathrm{PBE\text{-}sr},\mu}(\mathbf{r}) \\ &+ (1 - \gamma)V_x^{\mathrm{PBE}}(\mathbf{r}) + V_c^{\mathrm{PBE}}(\mathbf{r}). \end{aligned}$$ (3)

Among the widely used short-range screened hybrids, the Heyd-Scuseria-Ernzerhof (HSE06) [102, 103] functional is particularly notable, typically adopting fixed parameters $\alpha = 0.25$, $\gamma = 0$, and $\mu = 0.11$ Bohr^{-1}. However, alternative choices of α and μ have been explored in modified HSE like functionals [48, 51–53, 102, 104]. A crucial refinement for accurately capturing excitonic effects in bulk solids is the proper asymptotic treatment of the Coulomb tail [105]. This can be achieved by setting γ equal to the inverse of the high-frequency macroscopic static dielectric constant [83, 84, 86], where ϵ_∞ is the high-frequency macroscopic static dielectric function or ion-clamped static (optical) dielectric function. This dielectric-dependent hybrid (DDH) approach improves the description of electronic screening, but its transferability across different material systems remains an open challenge [100]. In practice, additional strategies may be necessary to determine optimal values of α, γ, and μ.

As evident from Eqs. 2 and 3, beyond the choice of α, accurate determination of ϵ_∞ and μ is critical for achieving predictive RSH calculations. Several methodologies exist to determine these parameters, which will be discussed in the following sections.

B. Strategies for determining the parameters and Present Consideration

First, we consider the bulk systems (for example, simple cubic bulk). A finite electronic field is applied to determine the dielectric tensor. Because the bulk system is homogeneous, it is straightforward to obtain the macroscopic dielectric constant as,

$$\epsilon_\infty^{\mathrm{3D}} = \frac{1}{3}\sum_{i=1}^{3}\epsilon_{\infty,i}^{\mathrm{3D}},$$

(4)

where $\epsilon_{\infty,i}^{\mathrm{3D}}$ $(i = 1, 2, 3)$ are the diagonal elements of the dielectric tensor. However, in layered materials, the dielectric response is anisotropic due to the coexistence of distinct materials within the system. Consequently, the assumption of homogeneity used for bulk solids is no longer valid. Because of this anisotropy of van der Waals (vdW) layer materials, the in-plane ($\parallel$) and out-of-plane ($\perp$) components of the dielectric tensor exhibit significant differences. In such cases, a more sophisticated approach is required to determine the dielectric response accurately.

In the following, we propose the construction of the parameters of the screened-DDH for two-dimensional vdW systems. Accurate calculation of the dielectric response requires the elimination of the vacuum contribution. For layered materials, the macroscopic static dielectric tensor is first calculated using a supercell approach with a sufficiently large vacuum layer to avoid the non-physical interaction between periodic repetitions of layers. The macroscopic dielectric tensor of the supercell (SC), ϵ_∞^{SC}

is determined using the reciprocal space expression [106–108],

$$\epsilon^{\mathrm{SC}}_{\mathbf{G},\mathbf{G}'}(\mathbf{q},\omega) = \delta_{\mathbf{G},\mathbf{G}'} - v_c \chi^{\mathrm{SC}}_{\mathbf{G},\mathbf{G}'}(\mathbf{q},\omega) . \quad (5)$$

where $v_c = \frac{4\pi}{|\mathbf{G}+\mathbf{q}||\mathbf{G}'+\mathbf{q}|}$ is the Hartree potential and

$$\chi^{\mathrm{SC}}_{\mathbf{G},\mathbf{G}'} = \chi^{0,\mathrm{SC}}_{\mathbf{G},\mathbf{G}'} + \chi^{0,SC}_{\mathbf{G},\mathbf{G}'}\left(v_c + f_{xc}(\mathbf{q},\omega)\right)\chi^{\mathrm{SC}}_{\mathbf{G},\mathbf{G}'} , \quad (6)$$

with $f_{xc}(\mathbf{q},\omega)$ being the XC kernel, $\chi^{SC}_{\mathbf{G},\mathbf{G}'}(\mathbf{q},\omega)$ is the reducible polarizability, and $\chi^{0}_{\mathbf{G},\mathbf{G}'}(\mathbf{q},\omega)$ being the irreducible polarizability matrix of the supercell. However, often the effect of $f_{xc}(\mathbf{q},\omega)$ is neglected and Eq. 5 is then referred as RPA. Our interest lies in the inverse of the macroscopic dielectric matrix $[\epsilon^{SC}_{\infty}(\mathbf{q},\omega)]^{-1}$, which is obtained from the head of the inversion of the full microscopic dielectric tensor as [106],

$$[\epsilon^{\mathrm{SC}}_{\infty}(\mathbf{q},\omega)]^{-1} = \lim_{\mathbf{q}\to0}[\epsilon^{\mathrm{SC}}_{0,0}(\mathbf{q},\omega)]^{-1} . \quad (7)$$

Typically, for layer 2D materials, the static microscopic dielectric tensor, $\epsilon^{\mathrm{SC}}_{\infty}$ has following matrix form,

$$\overleftrightarrow{\epsilon^{\mathrm{SC}}_{\infty}} = \begin{pmatrix} \epsilon^{\mathrm{SC}}_{\infty\parallel} & 0 & 0 \\ 0 & \epsilon^{\mathrm{SC}}_{\infty\parallel} & 0 \\ 0 & 0 & \epsilon^{\mathrm{SC}}_{\infty\perp} \end{pmatrix} . \quad (8)$$

where $\epsilon^{SC}_{\infty,\parallel}$ is the in-plane dielectric constant and $\epsilon^{\mathrm{SC}}_{\infty,\perp}$ is the out-of-plane dielectric constant of the supercell, which includes contributions from both the 2D material and the vacuum. Typically, the density functional perturbation theory (DFPT) [109] is used to calculate the susceptibility tensor of the supercell. We use RPA@PBE to determine the dielectric tensor where the local field effect is included within the Hartree approximation [106].

We adopt the following strategy to determine the dielectric constants for two-dimensional layer materials, including vacuum:

(i) We first calculate the supercell macroscopic dielectric constants ϵ^{SC}_{∞} for both the in-plane $\epsilon^{SC}_{\infty,\parallel}$ and out-of-plane $\epsilon^{SC}_{\infty,\perp}$ using RPA@PBE which includes contributions from both the 2D material and the vacuum.

(ii) The in-plane and out-of-plane dielectric constant for 2D materials is then obtained by rescaling the supercell dielectric constant as,

$$\begin{aligned} \epsilon^{\mathrm{2D}}_{\infty\parallel} &= 1 + \frac{c}{t}(\epsilon^{\mathrm{SC}}_{\infty\parallel} - 1) \\ \epsilon^{\mathrm{2D}}_{\infty\perp} &= \left[1 + \frac{c}{t}\left(\frac{1}{\epsilon^{\mathrm{SC}}_{\infty\perp}} - 1\right)\right]^{-1} . \end{aligned} \quad (9)$$

Here, c is the supercell height or length perpendicular to the 2D material layers, and t is the thickness of the 2D material layers (see Fig. 1 for details). The relation

of Eq. 9 is obtained from *principle of equivalent capacitance* [110, 111] (See Appendix A for details.) The important fact of this consideration is that the rescaled $\epsilon^{2D}_{\infty\parallel}$ and $\epsilon^{2D}_{\infty\perp}$ remain almost independent with the different supercell height, c. In all our calculations we consider $\epsilon_{vacuum} = 1$.

Note also for a free-standing monolayer or strict 2D limits, i.e., for large (infinite) separation between layers, that $\epsilon^{SC}_{\infty\parallel} \to 1$, $\epsilon^{SC}_{\infty\perp} \to 1$, resulting $\epsilon^{2D}_{\infty\parallel} \to 1$, $\epsilon^{2D}_{\infty\perp} \to 1$ [111]. But Eq. 9 is more valid and physical for finite thickness, which our present work uses to construct the DDH for 2D layer materials.

(iii) Finally, to solve the DDH equation, one needs to construct the effective dielectric constant, ϵ^{2D}_{∞}. The following choices can be adopted:

- For the bulk system, $c = t$, which corresponds to $\epsilon^{2D}_{\infty\parallel} = \epsilon^{SC}_{\infty\parallel}$, and $\epsilon^{2D}_{\infty\perp} = \epsilon^{SC}_{\infty\perp}$, implies the effective dielectric constants becomes the averaging over diagonal elements of the static dielectric tensor,

$$[\epsilon^{\mathrm{2D,\ eff}}_{\infty}]_{\mathrm{bulk}} = \frac{2\epsilon^{\mathrm{2D}}_{\infty\parallel} + \epsilon^{\mathrm{2D}}_{\infty\perp}}{3}. \quad (10)$$

where we assume $[\epsilon^{\mathrm{2D}}_{\infty\parallel}]_{xx} = [\epsilon^{\mathrm{2D}}_{\infty\parallel}]_{yy}$. Thus Eq. 10 is, in effect, the same as Eq. 4.

- However, for layers, such as monolayer or bilayer one has to consider different strategies for effective $\epsilon^{2D,eff}_{\infty}$. Following Appendix A, for a monolayer or bilayer of the 2D vdW material, we consider the effective dielectric constant as,

$$[\epsilon^{\mathrm{2D,\ eff}}_{\infty}]_{\mathrm{layers}} = \sqrt{\epsilon^{\mathrm{2D}}_{\infty\parallel}\epsilon^{\mathrm{2D}}_{\infty\perp}}. \quad (11)$$

Eventually, Eq. 11 is also used in refs. [68, 112] as the effective dielectric constant for Coulomb interaction in the plane for monolayer-TMDs.

We use Eq. 10 (in case of bulk) and Eq. 11 (in case of a monolayer) in our screened DDH potential (or exchange energy functional) to calculate the 2D vdW material properties. Finally, using Eq. 3, the generalized potential energy of the screened-exchange dielectric-dependent range-separated hybrid (SE-DD-RSH) becomes,

$$\begin{aligned} V^{\mathrm{SE\text{-}DD\text{-}RSH}}_{xc}(\mathbf{r},\mathbf{r}';\mu) = & \left[1 - \left(1 - [\epsilon^{\mathrm{2D,\ eff}}_{\infty}]^{-1}\right)\mathrm{erf}(\mu r)\right] V^{\mathrm{Fock}}_{x}(\mathbf{r},\mathbf{r}') \\ & - \left(1 - [\epsilon^{\mathrm{2D,\ eff}}_{\infty}]^{-1}\right) V^{\mathrm{PBE\text{-}sl},\mu}_{x}(\mathbf{r}) \\ & + \left(1 - [\epsilon^{\mathrm{2D,\ eff}}_{\infty}]^{-1}\right) V^{\mathrm{PBE}}_{x}(\mathbf{r}) + V^{\mathrm{PBE}}_{c}(\mathbf{r}) \quad (12) \end{aligned}$$

where we choose $\alpha = 1$ in Eq. 3. Here, the model dielectric function,

$$\epsilon_m = 1 - \left(1 - [\epsilon^{\mathrm{2D,\ eff}}_{\infty}]^{-1}\right)\mathrm{erf}(\mu r) . \quad (13)$$

For free-standing monolayer or strict 2D limit $\epsilon_\infty^{2D,\,eff} \rightarrow [\epsilon_\infty^{2D,\,eff}]_{layers} \rightarrow 1$, implies $\epsilon_m \rightarrow 1$. This also implies free-standing monolayer or strict 2D limit the long-range exchange potential $\sim \frac{1}{q^2}$.

Regarding μ, we consider $\mu = \mu_{bulk} = \mu_{eff}^{fit}$ from ref. [83, 84] for bulk, given by

$$\mu_{bulk} = \mu_{eff}^{fit} = \frac{a_1}{\langle r_s \rangle} + \frac{a_2 \langle r_s \rangle}{1 + a_3 \langle r_s \rangle^2} \,, \qquad (14)$$

with $a_1 = 1.91718$, $a_2 = -0.02817$, $a_3 = 0.14954$, and

$$\langle r_s \rangle = \frac{1}{V_{cell}} \int_{cell} \left(\frac{3}{4\pi(n_\uparrow(\mathbf{r}') + n_\downarrow(\mathbf{r}'))} \right)^{1/3} d^3 r' \,. \quad (15)$$

However, for the monolayer, the strategies of ref. [83, 84] are not convenient because of the involvement of the volume of the unit cell. In contrast, we consider the following function form to be useful,

$$\mu_{\text{layers}} = f \left(\left[\epsilon_\infty^{2D,\,eff} \right]_{\text{layers}}^{-1} \right). \qquad (16)$$

and out of the different forms proposed for bulk solids (see Table 1 in the refs. [98]), we consider the following generalized form with a fitting parameter for the 2D monolayer of the vdW systems,

$$\mu_{\text{layers}} = a N_e^{1/3} \left[1 - \left(\epsilon_\infty^{2D,\,eff} \right)_{\text{layers}}^{-1} \right]^{-1/2}. \qquad (17)$$

where N_e represents the number of the valence electrons. For instance, in the case of MoX$_2$ or WX$_2$ ($X = S/Se/Te$) $N_e = N_e^{Mo/W} = 6$; for InSe, $N_e = N_e^{In} = 3$, and for hexagonal boron nitride (hBN), $N_e = N_e^B = 3$. The parameter, $a = 0.3$ is obtained from fitting with the reference G_0W_0 band gap data and provides a well-balanced estimation of the band gap across various monolayer materials. As stated before, we also note that Eq. 17 is also used previously in the case of bulk solids [98], which is modified or scaled by a in the present case for application to the lower-dimensional materials. Once the parameter a is determined and fixed, no additional fitting is required for other systems outside the test set. Since μ_{layers} depends solely on the dielectric constant of 2D systems (assuming a remains fixed), it can be readily evaluated without further fitting.

C. Other recent strategies

We also recall some recent progress in constructing the screened-exchange functionals for 2D materials, such as,

(a) For heterogeneous systems such as interfaces and surfaces, Zhan et al. [82] proposed the same form as Eq. 12, but a local, spatially-dependent mixing fraction, $\gamma(\mathbf{r}, \mathbf{r}')$ is used,

$$\gamma(\mathbf{r}, \mathbf{r}') = \frac{1}{\sqrt{\epsilon_\infty(\mathbf{r}) \epsilon_\infty(\mathbf{r}')}} = \frac{1}{\sqrt{\epsilon_\infty^{2D}(\mathbf{r}, \mathbf{r}')}} \,, \qquad (18)$$

with $\epsilon_\infty(\mathbf{r})$ being the local dielectric function. Their screened-exchange range-separated hybrid (SE-RSH) also takes the form $\alpha = 1$, and $\mu = \mu(\mathbf{r})$ is also a position-dependent function, and it is obtained in a self-consistent manner [82]. The screened-dielectric function proposed by Zhan et al. [82] is fully nonempirical, and all the parameters are position-dependent. Notably, the SE-RSH function is the most generalized form, suitable for complex materials such as bulk, heterogeneous materials, interfaces, and two-dimensional layered solids. The cost has to be paid in terms of an extra effort to implement the more complex local dielectric function, $\epsilon(\mathbf{r})$, and the local screening function $\mu(\mathbf{r})$. We recall that the local dielectric function is determined in real space using the Wannier basis.

(b) An optimal tuning of parameters related to the two-dimensional vdW systems is proposed in various papers published by Ramasubramaniam et al. [74, 100]. This is based on two main facts: (i) Because $\epsilon_\infty(q)$ tends to $\epsilon_\infty(q) = 1 + \mathcal{O}(q)$ for a strict 2D limit [113], using Eq. 3, the potential energy functional of their screened-range-separated hybrid (SRSH) looks like

$$\begin{aligned} V_{xc}^{SRSH}(\mathbf{r}, \mathbf{r}', \alpha; \mu) &= \alpha[1 + \text{erf}(\mu r)] V_x^{\text{Fock}}(\mathbf{r}, \mathbf{r}') \\ &+ (1 - \alpha) V_x^{\text{PBE-sr},\mu}(\mathbf{r}) + V_c^{\text{PBE}}(\mathbf{r}) \end{aligned} \quad (19)$$

(ii) In Eq. 19, then a scanning over the $\alpha - \mu$ parameters is performed such that the corresponding SRSH band gaps match with the reference quasi-particle G_0W_0 result by imposing the constraints that the difference between the quasiparticle band gaps and SRSH band gaps at a particular K point becomes optimal, i.e.,

$$\Delta E_g^{\alpha,\mu} = \arg \min_{\alpha,\mu} |E_g^{G_0W_0} - E_g^{SRSH}|. \qquad (20)$$

As noted from ref. [74], the corresponding pairs of α and μ are not unique and depend on the materials. Furthermore, the previous band gap calculations of the quasiparticle GW are required. However, as also noted in ref. [74], a unique or optimal set of parameters (α^*, μ^*) is obtained by simultaneously optimizing the bulk and monolayer band gap by imposing the constraint of Eq. 20, which is ultimately used to compute the electronic and optical properties of 2D vdW materials. Other than this optimal tuning procedure, very recently, a non-empirical screened range-separated hybrid functional is also proposed using a Wannier-localized optimally-tuned procedure [114].

In the present scenario, our proposed method takes the same form as that of Zhan et al. [82], only instead of the non-local $\epsilon^{-1}(\mathbf{r}, \mathbf{r}')$, we have used $\epsilon_\infty^{2D,eff}$, a fixed effective value. Thus, the present method can be thought of as similar to the most generalized form of ref. [82]. Moreover, the present approach differs from case (ii) in that, for bulk systems, our method is entirely non-empirical, whereas for 2D layered systems, only the dielectric constant ϵ is required, assuming $a = 0.3$ is fixed to a specific value.
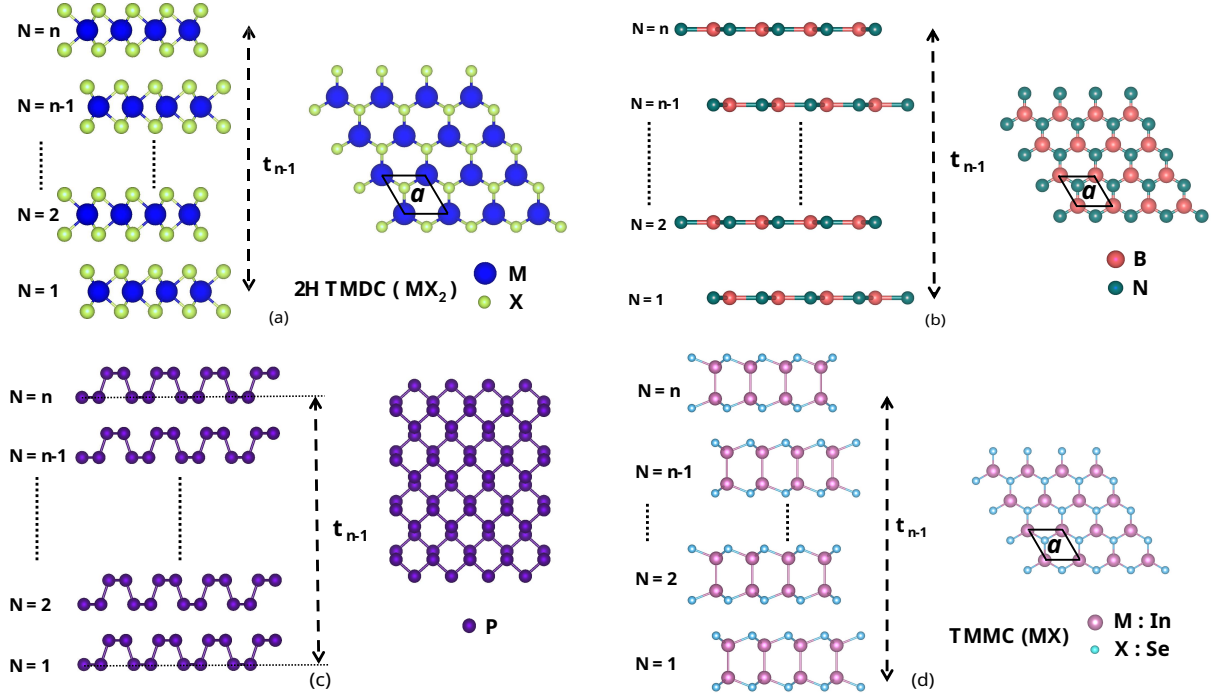
FIG. 1. Multilayer AB staking configuration of 2H TMDC of MX_2 (a), AA' stacking of hBN (b), AB stacking of BP (c), and AB stacking of $\beta-$InSe (d). Here, a is the in-plane lattice constant, and t_{n-1} is the thickness (or the distance) between the metal atoms of $n+1$ layers when n layers are considered.

III. RESULTS AND DISCUSSIONS

A. Materials and computational details

We investigate the electronic and optical properties of nine van der Waals (vdW) materials, encompassing bulk and monolayer, from the families of transition metal dichalcogenides (TMDCs), hexagonal boron nitride (hBN), black phosphorus (BP), and transition metal monochalcogenides (TMMCs). Specifically, we examine the trigonal prismatic (2H) phases of MoS_2, $MoSe_2$, $MoTe_2$, WS_2, WSe_2, and WTe_2, collectively referred to as MX_2. Both monolayer and bulk structures are modeled using the conventional AB stacking configuration for TMDCs and AA' stacking for hBN. Black phosphorus, an orthorhombic group-IV monochalcogenide, is also included due to its intriguing anisotropic transport properties and strong excitonic effects [115, 116]. We consider both the monolayer (phosphorene) and bulk structures, adopting an AB stacking order. Finally, we explore β-InSe as a representative TMMC system, where the group IIIA element (In) forms a hexagonal lattice with chalcogen (Se) atoms. A summary of the structural configurations is provided in Fig. 1.

All calculations are performed using the plane-wave pseudopotential code Vienna Ab initio Simulation Package (VASP) [117–120]. Structural optimizations are carried out using the Perdew-Burke-Ernzerhof (PBE) exchange-correlation functional with the D3(0) dispersion correction. The equilibrium volume of bulk structures is first determined at the PBE+D3(0) level, after which the optimized in-plane lattice constants are used to construct corresponding monolayer geometries. Monolayer structures are further relaxed with fixed out-of-plane parameters to capture intrinsic strain effects. Electronic band structure calculations are performed on PBE-relaxed geometries using a plane-wave energy cutoff of 650 eV. For quasi-particle band gap corrections, we employ the G_0W_0 approach with a PBE starting point, except for bulk BP, where the HSE06 hybrid functional is used. The macroscopic static dielectric tensor ϵ_∞^{SC} (both in-plane and out-of-plane components) is computed within the random phase approximation (RPA) at the PBE level (RPA@PBE), except for bulk BP, where RPA@HSE06 is applied. The optical spectra within the Bethe-Salpeter equation (BSE) and time-dependent density functional theory (TDDFT) formalisms are computed using a Gaussian broadening of $\sigma = 0.1$ eV. The **k**-point sampling grids used for all calculations are provided in Table I.

Further details on the computational parameters are available in Appendix B. The structural configurations and stacking arrangements of the materials under consideration are illustrated in Fig.1.

TABLE I. Direct band gaps (eV) of bulk and monolayer vdW materials. For MoX_2, WX_2, and hBN, the direct band gaps are computed at the $K_v \to K_c$ transition; while for BP and InSe, at $\Gamma_v \to \Gamma_c$ is considered. Spin-orbit coupling (SOC) effects, derived from PBE, are subtracted across methods. Values in parentheses indicate deviations from corresponding G_0W_0 results.

Material	Transition	k-points	$\gamma = [\epsilon_\infty]^{-1}$	μ (Å^{-1})	E_g^{PBE}	E_g^{HSE06}	$E_g^{SE-DD-RSH}$	$E_g^{G_0W_0}$	ΔSOC[b]	
					Bulk					
MoS_2	$K_v \to K_c$	$12 \times 12 \times 4$	0.0867	1.739	1.69 (-0.46)	2.14 (0.00)	2.10 (-0.04)	2.14	0.03	
$MoSe_2$	$K_v \to K_c$	$12 \times 12 \times 4$	0.0760	1.720	1.50 (-0.54)	1.94 (-0.10)	1.86 (0.02)	1.88	-0.03	
$MoTe_2$	$K_v \to K_c$	$12 \times 12 \times 4$	0.0612	1.720	1.13 (-0.51)	1.55 (-0.08)	1.42 (0.00)	1.42	-0.05	
WS_2	$K_v \to K_c$	$12 \times 12 \times 4$	0.0946	1.814	1.67 (-0.54)	2.15 (-0.06)	2.12 (-0.09)	2.21	0.19	
WSe_2	$K_v \to K_c$	$12 \times 12 \times 4$	0.0803	1.757	1.33 (-0.50)	1.82 (-0.01)	1.71 (-0.12)	1.83	0.22	
WTe_2	$K_v \to K_c$	$12 \times 12 \times 4$	0.0615	1.739	0.81 (-0.35)	1.22 (0.06)	1.10 (-0.06)	1.16	0.28	
hBN	$K_v \to K_c$	$12 \times 12 \times 4$	0.2561	1.537	4.96 (-1.68)	6.43 (-0.21)	7.59 (0.94)	6.64 (7.32[a])	0.00	
BP	$\Gamma_v \to \Gamma_c$	$9 \times 9 \times 4$	0.1080	1.587	0.03 (-0.68)	0.52 (-0.18)	0.49 (-0.22)	0.71	0.00	
InSe	$\Gamma_v \to \Gamma_c$	$9 \times 9 \times 4$	0.1137	1.285	0.38 (-0.93)	1.10 (-0.21)	1.21 (-0.15)	1.32	0.03	
					Layers					
MoS_2	$K_v \to K_c$	$15 \times 15 \times 1$	0.1144	1.095	1.70 (-0.85)	2.16 (-0.39)	2.31 (-0.24)	2.55	0.08	1L
			0.1076	1.091	1.70 (-0.66)	2.15 (-0.21)	2.28 (-0.08)	2.36	0.04	2L
$MoSe_2$	$K_v \to K_c$	$15 \times 15 \times 1$	0.0996	1.086	1.48 (-0.75)	1.93 (-0.30)	2.03 (-0.20)	2.23	0.11	1L
			0.0930	1.082	1.48 (-0.58)	1.93 (-0.13)	2.00 (-0.06)	2.06	0.06	2L
$MoTe_2$	$K_v \to K_c$	$15 \times 15 \times 1$	0.0768	1.072	1.07 (-0.61)	1.51 (-0.17)	1.54 (-0.14)	1.68	0.13	1L
			0.0707	1.069	1.08 (-0.45)	1.50 (-0.03)	1.51 (-0.02)	1.53	0.08	2L
WS_2	$K_v \to K_c$	$15 \times 15 \times 1$	0.1206	1.099	1.72 (-1.01)	2.21 (-0.52)	2.42 (-0.32)	2.73	0.26	1L
			0.1153	1.095	1.73 (-0.81)	2.21 (-0.33)	2.40 (-0.14)	2.54	0.21	2L
WSe_2	$K_v \to K_c$	$15 \times 15 \times 1$	0.1052	1.089	1.42 (-0.88)	1.89 (-0.41)	2.02 (-0.28)	2.30	0.29	1L
			0.0996	1.086	1.43 (-0.71)	1.89 (-0.25)	2.00 (-0.14)	2.14	0.24	2L
WTe_2	$K_v \to K_c$	$15 \times 15 \times 1$	0.0800	1.074	0.90 (-0.70)	1.33 (-0.27)	1.37 (-0.23)	1.60	0.32	1L
			0.0741	1.071	0.91 (-0.54)	1.32 (-0.13)	1.33 (-0.12)	1.45	0.25	2L
hBN	$K_v \to K_c$	$15 \times 15 \times 1$	0.3043	0.980	4.70 (-2.72)	6.11 (-1.31)	8.35 (0.94)	7.42 (8.32[a])	0.00	1L
			0.3001	0.977	4.74 (-2.36)	6.15 (-0.94)	8.38 (1.28)	7.10 (7.87[a])	0.00	2L
BP	$K_v \to K_c$	$15 \times 15 \times 1$	0.1046	1.024	0.67 (-0.84)	1.32 (-0.19)	1.48 (-0.03)	1.51	0.00	1L
			0.0767	1.009	0.29 (-0.60)	0.88 (-0.01)	0.90 (0.01)	0.89	0.00	2L
InSe	$K_v \to K_c$	$15 \times 15 \times 1$	0.1507	0.887	1.71 (-1.32)	2.49 (-0.55)	3.22 (0.18)	3.04	0.05	1L
			0.1416	0.882	1.16 (-1.09)	1.87 (-0.38)	2.50 (0.25)	2.25	0.02	2L

[a] partially self-consistent GW ($scGW_0$) calculation.
[b] $\Delta SOC = E_g^{PBE} - E_g^{PBE-SOC}$

B. Layer-dependent band gaps

We systematically evaluate the performance of various density functional theory (DFT) methods for predicting electronic band gaps, as summarized in Table I. Standard functionals such as PBE and HSE06 are included for benchmarking purposes. In the absence of experimental band gap data, single-shot G_0W_0 calculations serve as the reference standard for assessing the accuracy of different methodologies.

The performance of the SE-DD-RSH functional is first benchmarked for bulk materials using the effective dielectric constant, $\epsilon_\infty^{2D,eff}$, derived from Eq. 10. For MX_2, WX_2, and hBN, we report direct band gaps at the K point, whereas for β-InSe and black phosphorus (BP), the gaps are reported at the Γ point. As expected, PBE significantly underestimates the band gaps of all bulk systems. Both HSE06 and SE-DD-RSH provide improved predictions for MX_2 and WX_2, yielding results that closely align with G_0W_0 calculations.

For the wide-bandgap insulator hexagonal boron ni-

tride (hBN), SE-DD-RSH slightly overestimates the band gap compared to G_0W_0. However, recent studies have emphasized the importance of zero-point renormalization (ZPR) corrections in refining band gap estimates [121]. By incorporating a ZPR correction of $\sim$ 0.3 eV from Ref.[121], the SE-DD-RSH band gap is adjusted to approximately 7.30 eV, bringing it into closer agreement with values reported at various levels of theory. Furthermore, we explore the performance of partially self-consistent GW calculations ($scGW_0$), where the Green's function G is iterated self-consistently while keeping the screened Coulomb interaction W and the orbitals fixed at the PBE level. As shown in Table I, the $scGW_0$ band gap for hBN is 7.32 eV, demonstrating close agreement with SE-DD-RSH and further highlighting the variability introduced by different levels of self-consistency in GW methods.

Black phosphorus (BP), on the other hand, is a narrow-bandgap semiconductor with a G_0W_0 bandgap of 0.71 eV. Due to the metallic character predicted by PBE, G_0W_0 calculations are initialized from the HSE06 eigensystem.
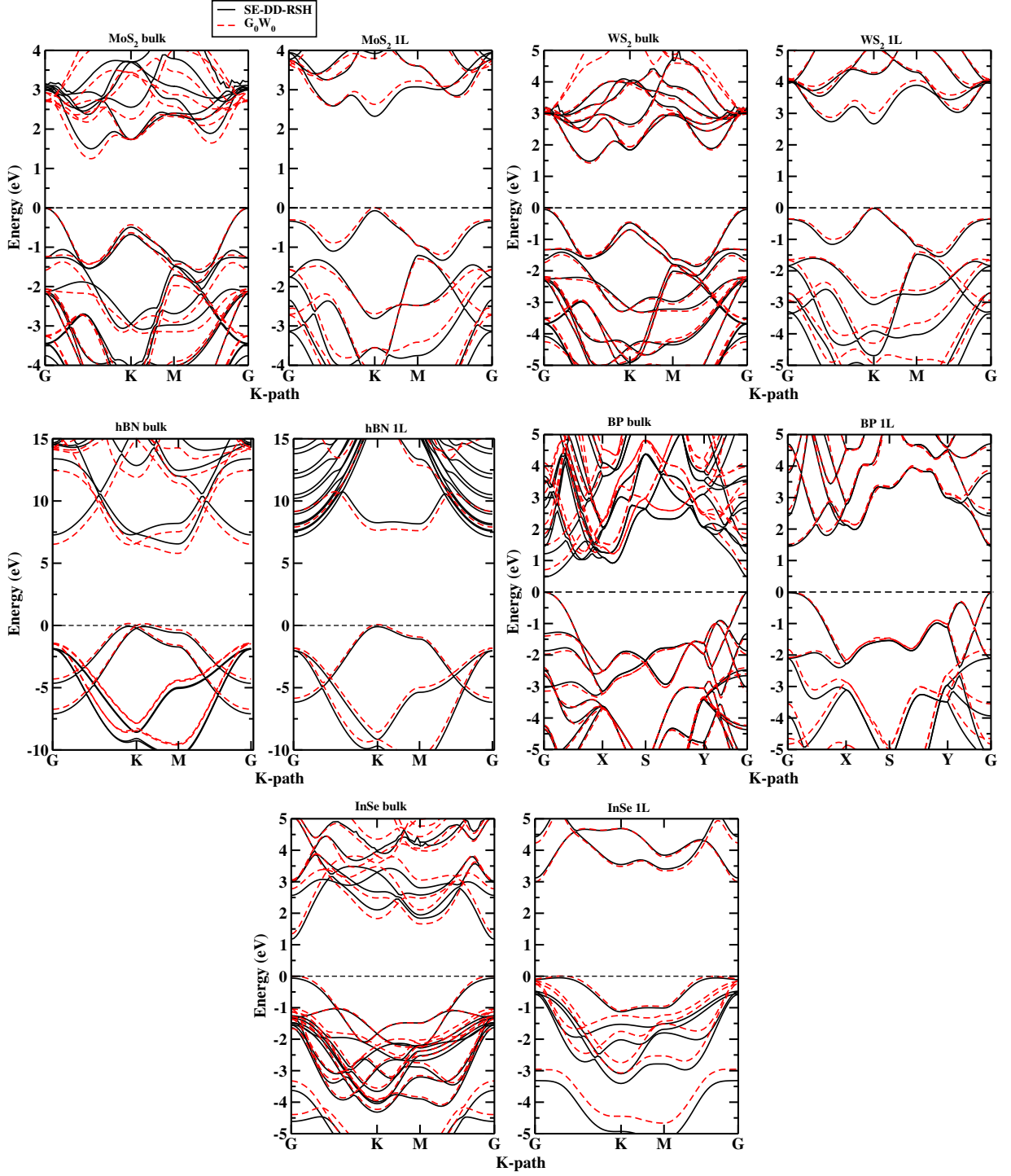
FIG. 2. band structures of MoS_2, WS_2, hBN, BP, and InSe as obtained from SE-DD-RSH and and G_0W_0. For bulk BP, G_0W_0 is calculated on top of the HSE06. Also, the SE-DD-RSH dielectric constant is calculated using HSE06 for this particular material.

For SE-DD-RSH, the dielectric screening parameter $\epsilon_\infty^{\mathrm{SC}}$ is computed using HSE06. We observe that both HSE06 and SE-DD-RSH yield similar band gaps within ~ 0.2 eV of G_0W_0. Similarly, for the 2H phase of β-InSe, which features a direct gap at Γ, G_0W_0 estimates a gap of 1.32 eV. SE-DD-RSH provides an improved prediction of 1.21 eV, outperforming HSE06. Notably, for bulk systems, the parameters for SE-DD-RSH are determined in a non-empirical manner, and the method performs very well in predicting band gaps.

Now, we turn to the performance of different methods for monolayers. For monolayers of transition-metal dichalcogenides (MoS$_2$, MoSe$_2$, MoTe$_2$, WS$_2$, WSe$_2$, and WTe$_2$), the PBE functional systematically underestimates the band gaps, with more pronounced errors than in bulk. While HSE06 provides an improvement, it still exhibits significant deviations from the precise values. In contrast, SE-DD-RSH demonstrates superior performance, closely reproducing G_0W_0 results across all monolayers (Table I), confirming that the physically motivated rescaling procedure (Eq.9) and range-separation parameter μ (Eq.17) appropriately capture the screening effects inherent to low-dimensional materials.

In the case of hBN, G_0W_0 predicts a band gap of 7.42 eV, while PBE and HSE06 significantly underestimate this value. SE-DD-RSH provides a band gap of 8.35 eV, which, despite a slight overestimation, aligns closely with $scGW_0$. This suggests that the G_0W_0 approach, while widely regarded as a state-of-the-art, retains some degree of empiricism and sensitivity to methodological approximations. Additionally, as noted in Ref. [121], incorporating a ZPR correction of 0.38 eV further improves the agreement between SE-DD-RSH and G_0W_0.

For phosphorene, the monolayer of black phosphorus (BP), G_0W_0 predicts a band gap of 1.51 eV, with PBE yielding an underestimated value of 0.67 eV. SE-DD-RSH provides a highly accurate prediction of 1.48 eV, while HSE06 underestimates the gap at 1.32 eV. Similarly, as a second set of examples, monolayer β-InSe with the 2H structure, G_0W_0 estimates a band gap of 3.04 eV, while SE-DD-RSH predicts 3.22 eV, demonstrating an excellent agreement. In contrast, HSE06 significantly underestimates the gap, predicting a value of 2.49 eV, further highlighting the limitations of fixed hybrid functionals for low-dimensional systems.

Next, moving to the bilayer structures, a similar trend is observed across different levels of approximation. SE-DD-RSH consistently outperforms HSE06, providing band gaps in closer agreement with G_0W_0 across all materials. The observed trends reinforce the limitations of HSE06 in describing 2D systems, as its fixed screening parameter ($\alpha = 0.25$) fails to account for the dimensionality-dependent dielectric response [30, 31]. This limitation, widely acknowledged in previous studies [29, 54], makes HSE06 unsuitable for simultaneously capturing both bulk and monolayer properties. In contrast, SE-DD-RSH emerges as a robust alternative, offering improved accuracy across different dimensionalities without the need for empirical adjustments.

For a comprehensive assessment, Fig. 2 compares the band structures of bulk and monolayer MoS$_2$, WS$_2$, hBN, BP, and InSe obtained from G_0W_0 and SE-DD-RSH. SE-DD-RSH accurately reproduces G_0W_0 band structures for bulk materials, with the exception of hBN. For monolayers, SE-DD-RSH maintains strong agreement with G_0W_0, further validating its effectiveness in capturing the dielectric screening effects that dominate low-dimensional materials.

C. Linear dielectric response

Next, we investigate the dielectric response and optical absorption spectra of bulk, monolayer, and bilayer structures of MX$_2$, WX$_2$, hBN, BP, and InSe, employing time-dependent SE-DD-RSH (TD-SE-DD-RSH) and benchmark our findings against Bethe-Salpeter equation calculations within the BSE@G_0W_0. The optical excitations are computed using linear-response time-dependent density functional theory (LR-TDDFT) by solving the Casida/BSE equation [124] with generalized Kohn-Sham (gKS) orbitals and eigenvalues. Within the Tamm-Dancoff approximation, transition matrix elements are systematically evaluated following Refs. [105, 124–126], ensuring a rigorous description of many-body interactions and excitonic effects across different dimensionalities. We consider the excitonic Hamiltonian,

$$A_{ai;bj} = \omega_{ai}\delta_{ij;ab} + \langle ib|\hat{K}|aj \rangle \qquad (21)$$

where $\omega_{ai} = \varepsilon_a - \varepsilon_i$ represents the energy difference between unoccupied (a, b) and occupied (i, j) are the occupied states within the gKS framework. The interaction term $\langle ib|\hat{K}|aj \rangle$ determines the nature of excitonic effects and takes distinct forms within TDDFT and BSE:

$$\langle ib|\hat{K}|aj \rangle = 2\langle ib|\hat{V}_H|aj \rangle - \langle ib|\hat{W}|ja \rangle , \qquad (22)$$

where the Hartree term V_H is universal. For TDDFT, the screened exchange interaction is expressed as

$$\langle ib|W|ja \rangle = \langle ib|f_{xc}^{non-local}|ja \rangle - \langle ib|f_{xc}^{local}|aj \rangle \quad (23)$$

with non-local XC kernel, $f_{xc}^{non-local}$ becomes Fock exchange term screened by dielectric function, $[\epsilon_\infty^{2D,eff}]^{-1}$ i.e., $\langle ib|f_{xc}^{non-local}|ja \rangle = \langle ib|[\epsilon_\infty^{2D,eff}]^{-1}\hat{V}_{Fock}|ja \rangle$ and the local XC kernel in TD-DFT calculation is given by $\langle ib|f_{xc}^{local}|aj \rangle$, where

$$f_{xc}^{local}(\mathbf{r}, \mathbf{r}') = \frac{\delta^2[E_c^{PBE} + (1 - [\epsilon_\infty^{2D,eff}]^{-1})E_x^{PBE}]}{\delta n(\mathbf{r})\delta n(\mathbf{r}')} \quad (24)$$

In contrast, BSE incorporates a dynamically screened interaction $\hat{W}(\omega)$, making the resulting excitation spectra more physically accurate. However, due to its computational expense, dynamical effects are often approximated or neglected.

Finally, the optical response within TDDFT and BSE is obtained from the imaginary part of the macroscopic dielectric function $\epsilon_2(\omega)$ as [126],

$$\epsilon_2(\omega) = \Im \left\{ \lim_{q \to 0} \epsilon^M(q, \omega) \right\} , \qquad (25)$$

Note that for layer materials, $\epsilon_2(\omega)$ is averaged over the in-plane components $\epsilon_2(\omega) = \frac{\epsilon_{xx}(\omega) + \epsilon_{yy}(\omega)}{2}$, while for bulk systems, a three-dimensional average is taken $\epsilon_2(\omega) = \frac{\epsilon_{xx}(\omega) + \epsilon_{yy}(\omega) + \epsilon_{zz}(\omega)}{3}$. For computational feasibility, spin-orbit coupling (SOC) effects are neglected, though their
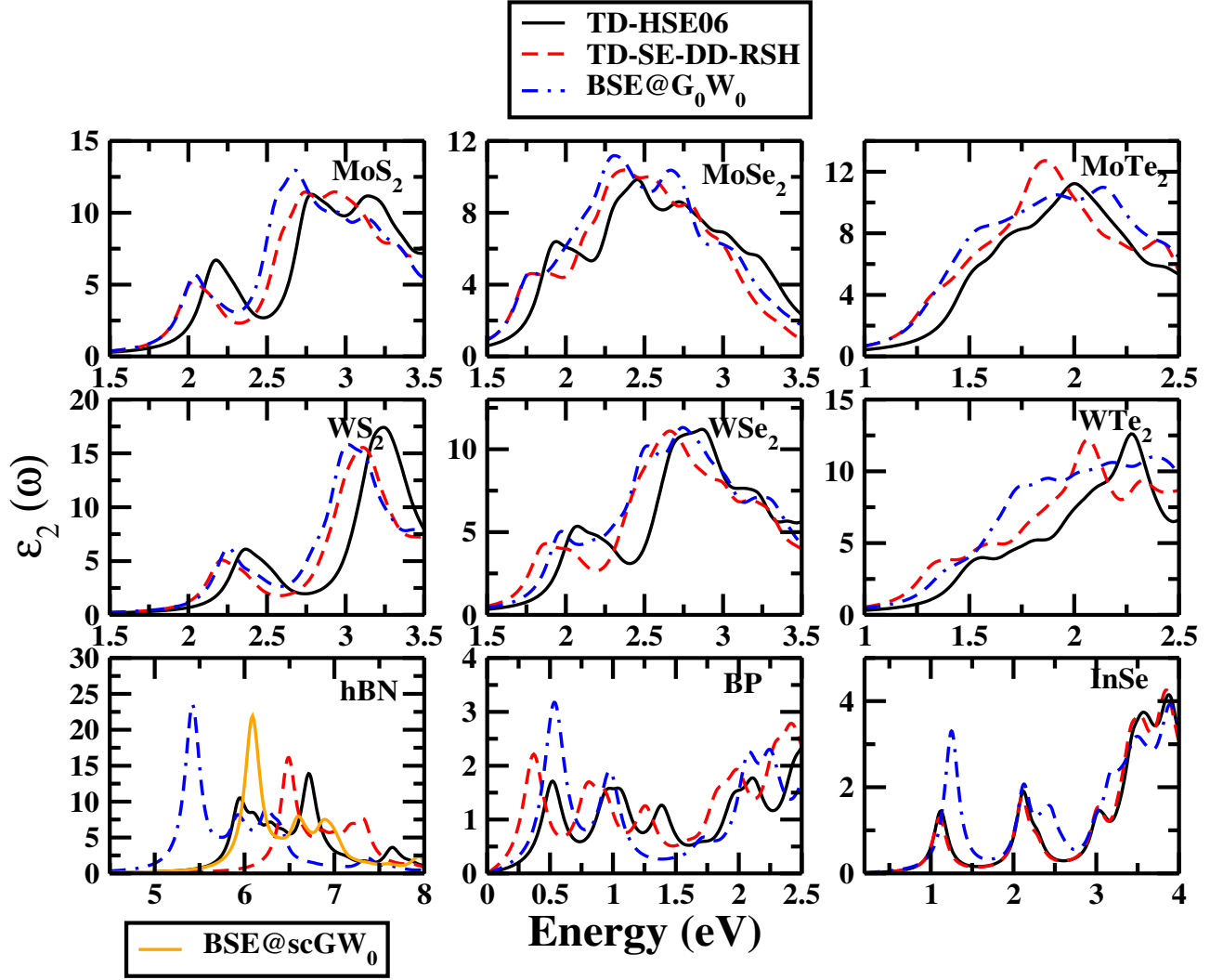
FIG. 3. Optical absorption spectra of bulk vdW materials obtained using different methods.

TABLE II. BSE and TDDFT spectral position or excitonic optical transitions and the exciton binding energies $\Delta = E_g^{G_0W_0/DFT} - E^{BSE/TDDFT}$ of the lowest bound excitons of bulk materials. Reported values are without SOC correction. All values are in eV.

Solids	MBPT		HSE06		SE-DD-RSH	
	BSE	Δ	TDDFT	Δ	TDDFT	Δ
MoS_2	2.03	0.145	2.15	0.023	2.01	0.121
$MoSe_2$	1.76	0.091	1.89	0.024	1.74	0.096
$MoTe_2$	1.30	0.071	1.48	0.022	1.30	0.071
WS_2	2.25	0.158	2.33	0.018	2.19	0.123
WSe_2	1.96	0.090	2.03	0.011	1.84	0.093
WTe_2	1.37	0.064	1.48	0.018	1.32	0.055
hBN	5.35 (6.00[a])	1.291 (1.320[b])	5.88	0.547	6.40	1.185
BP	0.53	0.174	0.52	0.006	0.37	0.117
InSe	1.25	0.093	1.12	0.010	1.10	0.140

[a] partially self-consistent GW ($scGW_0$) calculation.
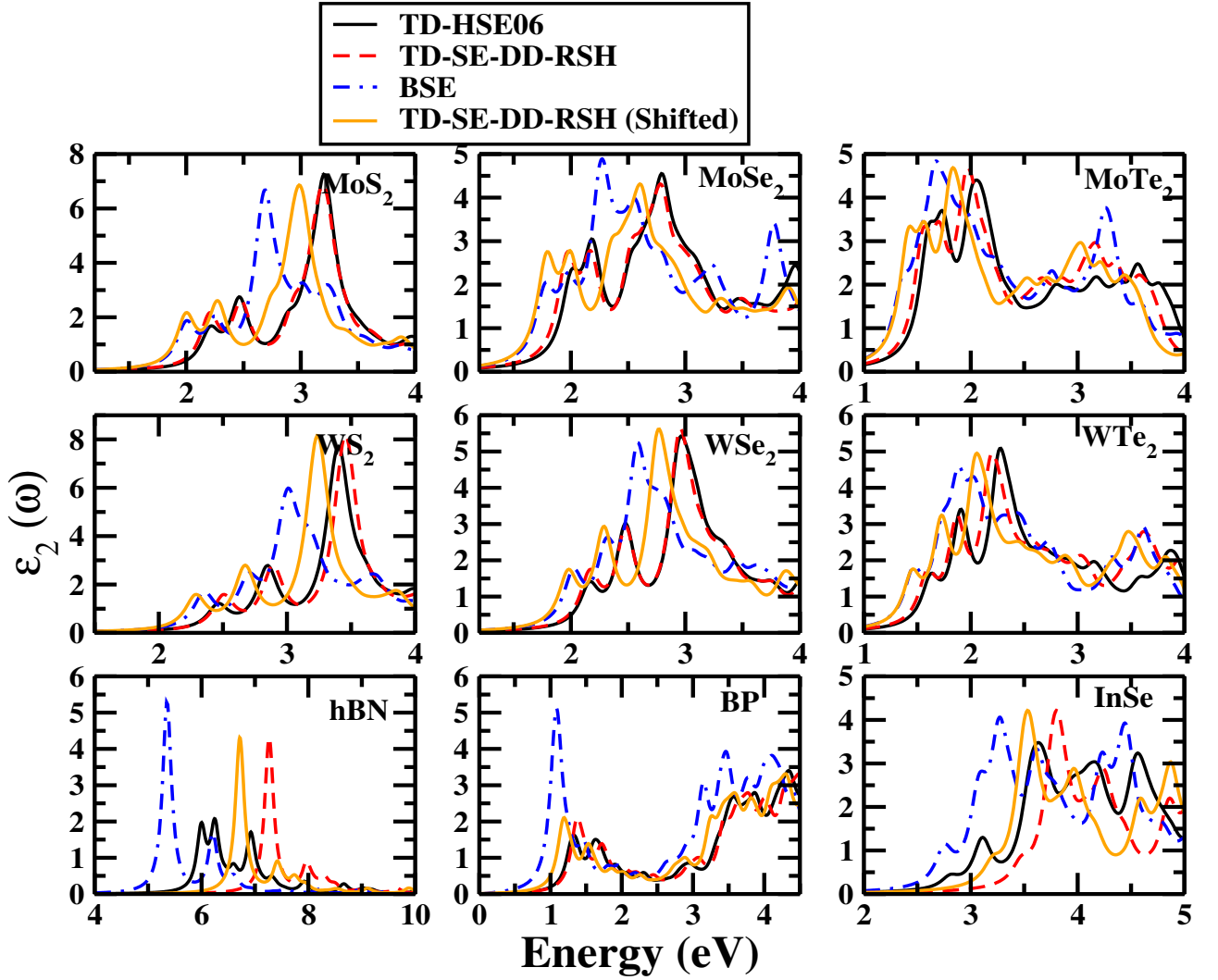[b] $\Delta = scGW_0$-BSE@$scGW_0$.

FIG. 4. Same as Fig. 3 but for monolayer vdW materials. The 'shifted' method refers to the empirical shifting on top of the DDH spectra.

influence is minor. Additionally, Table II and Table III, we present the peak positions obtained from TDDFT and BSE calculations, along with their respective deviations from the corresponding direct band gaps.

Figure 3 presents the optical absorption spectra for bulk van der Waals materials, revealing the efficacy of the TD-SE-DD-RSH approach in accurately capturing excitonic effects. As illustrated in both Fig.3 and TableII, the optical response predicted by TD-SE-DD-RSH exhibits remarkable agreement with the many-body perturbation theory (MBPT) results obtained using the Bethe-Salpeter equation atop G_0W_0 (BSE@G_0W_0). For instance, in the case of MoS_2, the TD-SE-DD-RSH optical gap, corresponding to the first excitonic peak, is computed at 2.01 eV, in excellent agreement with the BSE@G_0W_0 result of 2.03 eV. Similarly, for $MoSe_2$ and $MoTe_2$, the peak positions predicted by TD-SE-DD-RSH are 1.74 eV and 1.30 eV, respectively, closely matching the corresponding BSE@G_0W_0 values of 1.76 eV

and 1.30 eV. The deviations remain minimal across the transition-metal dichalcogenide (TMDC) family, with WS_2 and WSe_2 exhibiting discrepancies of merely ∼0.06 eV and ∼0.03 eV, respectively. This consistency extends to WTe_2, where the peak position deviation remains within ∼0.09 eV. From a theoretical standpoint, the exciton binding energy, defined as the difference between the optical excitation energy (TDDFT or BSE) and the quasiparticle band gap (or DFT)—emerges as a critical benchmark for validating the accuracy of computational approaches. Our analysis underscores the striking agreement between BSE@G_0W_0 and TD-SE-DD-RSH, reinforcing the latter's ability to encapsulate the intricate electron-hole interactions that govern the optical response of layered materials. In contrast, spectra computed using TD-HSE06 consistently deviate from BSE@G_0W_0 and TD-SE-DD-RSH, particularly underestimating exciton binding energies. This systematic discrepancy arises from the absence of long-range screened

TABLE III. BSE and TDDFT spectral position or excitonic optical transitions and the exciton binding energies $\Delta = E_g^{G_0W_0/DFT} - E^{BSE/TDDFT}$ of the lowest bound excitons of monolayers and bilayers. All calculations are without considering SOC.

Solids	MBPT		HSE06		SE-DD-RSH				Layers
	BSE	Δ	TDDFT	Δ	TDDFT	Δ	TDDFT+Shift	(TDDFT+Shift)$-$BSE	
MoS_2	2.00	0.630	2.21	0.029	2.20	0.188	2.00	-0.002	1L
	2.01	0.397	2.18	0.011	2.17	0.154	1.98	-0.032	2L
$MoSe_2$	1.77	0.564	2.00	0.037	1.97	0.169	1.79	0.011	1L
	1.78	0.344	1.98	0.014	1.93	0.131	1.77	-0.009	2L
$MoTe_2$	1.36	0.457	1.60	0.042	1.55	0.123	1.41	0.056	1L
	1.32	0.289	1.55	0.026	1.50	0.087	1.37	0.051	2L
WS_2	2.35	0.643	2.46	0.015	2.51	0.176	2.29	-0.065	1L
	2.34	0.413	2.43	0.002	2.46	0.153	2.25	-0.088	2L
WSe_2	2.02	0.572	2.16	0.017	2.17	0.150	1.98	-0.045	1L
	1.99	0.382	2.12	0.004	2.12	0.120	1.94	-0.056	2L
WTe_2	1.46	0.458	1.62	0.023	1.59	0.100	1.45	-0.011	1L
	1.41	0.295	1.57	0.003	1.53	0.081	1.39	-0.018	2L
hBN	5.35	2.064	5.99	0.111	7.26	1.090	6.71	1.363	1L
	5.33	1.767	6.01	0.148	7.21	1.168	6.67	1.342	2L
BP	1.08	0.428	1.29	0.031	1.37	0.118	1.18	0.097	1L
	0.64	0.245	0.85	0.028	0.82	0.074	0.68	0.040	2L
InSe[a]	2.68	0.403	2.53	0.003	3.11	0.158	2.84	0.158	1L
	2.02	0.259	1.90	-0.003	2.42	0.107	2.16	0.147	2L

[a] Experimental exciton peak at 2.92 eV [122].

exchange in HSE06, leading to an incorrect asymptotic behavior of the exchange potential.

A notable exception to the observed agreement is found in hexagonal boron nitride (hBN), where the TD-SE-DD-RSH exciton peak appears at 6.40 eV—approximately 1 eV higher than the BSE@G_0W_0 value. This deviation is indicative of the well-documented challenges associated with accurately predicting the band gap of wide-gap insulators within conventional electronic structure formalisms [121]. However, previous theoretical investigations [121] report exciton peak energies in the range of 6.00 eV to 6.52 eV, depending on the self-consistency level of the underlying MBPT treatment. Additionally, the importance of ZPR effects in hBN has been emphasized, with an estimated correction of ~0.3 eV [121]. Incorporating this ZPR correction into our TD-SE-DD-RSH result yields a renormalized excitonic peak at ~6.10 eV, bringing it closer to experimental measurements (5.99 eV)[127] and advanced self-consistent many-body calculations such as $scGW_0$ (Table II).

A similar assessment for black phosphorus (BP) reveals a systematic deviation of ~0.2 eV between TD-SE-DD-RSH and BSE@G_0W_0, further confirming the former's reliability in describing excitonic effects in anisotropic layered semiconductors. Notably, for InSe, the first optical peak exhibits a marginal ~0.1 eV discrepancy between TD-SE-DD-RSH and BSE, emphasizing the robustness of the dielectric-dependent hybrid approach across different material classes.

Overall, while the HSE06 hybrid functional provides a reasonable estimate for quasiparticle band gaps, it systematically underestimates exciton binding energies due to the absence of nonlocal dielectric screening effects. This behavior is inherently linked to its formulation, which includes only short-range Hartree-Fock exchange, thereby failing to reproduce the correct asymptotic behavior of the screened exchange potential.

Regarding the optical absorption spectrum of monolayers, Fig. 4 provides a comparative analysis of various theoretical approaches in capturing excitonic effects. The spectral positions and exciton binding energies of the lowest bound excitons, summarized in Table III, reveal the profound impact of reduced Coulomb screening in low-dimensional systems. Unlike their bulk counterparts, monolayer materials exhibit significantly enhanced exciton binding energies due to the diminished dielectric screening, leading to stronger electron-hole interactions and more localized excitonic wavefunctions. Within this framework, the BSE@G_0W_0 formalism, which fully accounts for the frequency-dependent screening effects, remains the gold standard for computing exciton binding energies. Our analysis confirms that TD-SE-DD-RSH systematically approximates these values with high accuracy, whereas TD-HSE06 considerably underestimates exciton binding energies, often approaching zero. This discrepancy underscores the fundamental limitation of

TABLE IV. Comparison of band gaps and binding energies of theoretically obtained values (without SOC corrected) with experimental results. The experimental results are taken from Table II of ref. [123].

Solids	MBPT		SE-DD-RSH		Expt.	
	E_g	BE	E_g	BE	E_g	BE
MoS_2	2.63	0.63	2.39	0.188	2.15±0.06	0.2 (or 0.42)
					2.5	≥0.57
					2.47±0.08	0.44±0.08
					2.15±0.1	0.3
					2.17±0.1	0.31±0.04
$MoSe_2$	2.34	0.564	2.14	0.169	2.18	0.55
					2.15±0.06	0.5
WS_2	2.99	0.643	2.68	0.176	2.41±0.04	0.32±0.04
					2.7	0.7
					2.73	0.71±0.01
					3.01	0.929
					2.33±0.05	0.32±0.05
					2.38±0.06	0.36±0.06
					2.31−2 .53	0.26 - 0.48
WSe_2	2.59	0.572	2.31	0.150	2.02	0.37
					2.2±0.1	0.5
					2.35±0.2	0.6±0.2
					2.63	0.887
					2.08±0.1	0.4
					1.9	0.245

the HSE06 functional, which lacks the necessary long-range screened exchange to accurately describe excitonic states in two-dimensional (2D) materials. In contrast, TD-SE-DD-RSH provides a substantial improvement over TD-HSE06, capturing the essential screening physics while maintaining computational efficiency. For instance, in monolayer MoS_2, the spectral positions predicted by TD-SE-DD-RSH are systematically blueshifted by approximately 100 meV relative to TD-HSE06. This trend is consistently observed across other chalcogenide materials, reaffirming the robustness of the TD-SE-DD-RSH framework in 2D systems. Notably, for all TMDCs, the first bright excitonic peak is located at the K point of the Brillouin zone, in agreement with both theoretical and experimental studies.

Turning to the monolayer of hexagonal boron nitride (hBN), we find that the first excitonic peak position and corresponding exciton binding energy within TD-SE-DD-RSH are 7.26 eV and 1.09 eV, respectively. These values align closely with BSE@GW_0 results, highlighting the accuracy of our approach in capturing strong excitonic effects in wide-gap insulators. As discussed in prior theoretical works [72, 74], the determination of excitonic energies in hBN remains particularly challenging due to the

interplay of electronic correlation and ZPR effects. Recent studies [121] suggest that an additional ZPR correction may further refine the agreement with experimental measurements, underscoring the necessity of incorporating phonon-driven renormalization effects in future studies.

For the BP monolayer, our calculations indicate that the first excitonic peak obtained from BSE occurs at 1.08 eV, which is approximately 0.3 eV lower than the TD-SE-DD-RSH value at the Γ point. The corresponding exciton binding energies exhibit similar trends, with TD-SE-DD-RSH providing a significantly more accurate description than TD-HSE06. A similar performance is observed for monolayer InSe, where the first excitonic peak position obtained from TD-SE-RS-DDH (3.11 eV) is in close agreement with BSE@GW (2.68 eV). This prediction also aligns well with the experimentally measured optical gap of 2.92 eV [122], reinforcing the validity of TD-SE-RS-DDH as a computationally efficient alternative to many-body perturbation theory.

In principle, these discrepancies in linear optical absorption spectra between BSE and TDDFT arise primarily from differences in their treatment of the screening effects. Unlike G_0W_0, the conventional DFT and

TDDFT screened exchange kernel lacks frequency dependence, leading to systematic underestimations of exciton binding energies. To mitigate these discrepancies and provide a more realistic description of exciton peak positions, and hence the binding energies, in the following we propose a dielectric-dependent shited procedure to the TD-SE-DD-RSH optical spectra:

$$E^{TDDFT-Shifted} = E^{TDDFT} - a[\epsilon_\infty^{2D}]^{-1} \qquad (26)$$

$$E_b^{TDDFT-Shifted} = E_g^{SE-DD-RSH} - E^{TDDFT-Shifted}$$
$$= E_b^{TDDFT} + a[\epsilon_\infty^{2D}]^{-1} \qquad (27)$$

with a being the fitting parameter determined by comparison with BSE results, with an optimal value of 1.8 eV. The effectiveness of this shifted-TD-SE-DD-RSH method is demonstrated in Fig. 4 and Table III, where the corrected exciton peak positions and binding energies exhibit remarkable agreement with BSE@G_0W_0. Conceptually, this correction is analogous to the scissor operator approach commonly employed in quasiparticle band gap corrections, where the difference between the quasiparticle and Kohn-Sham band gaps dictates the magnitude of the shift.

Finally, in Table IV, we compare the theoretical values with available experimental results. The experimental data were obtained at different temperatures and on various exfoliated surfaces. Despite these variations, the trends indicate that both the G_0W_0 and SE-DD-RSH band gaps fall within the range of the experimental values. However, the binding energies obtained from TD-SE-DD-RSH are underestimated, although, for some systems, they remain within the lower limit of the experimental range.

High exciton binding energies from BSE for monolayers and bilayers indicate that its wavefunction is more localized than TD-SE-DD-CAM. In order to understand this in Fig. 5 we plot squared modulus of exciton amplitude $|\sum_{e,h} A_{e,h}^\Lambda(\mathbf{k})|^2$ for $e-h$ pair with $\Lambda = 1$ i.e., first bright exciton. The size of the projected circle denotes the absolute amplitude. As shown in Fig. 5, for this particular example of MoS$_2$ monolayer the BSE amplitude becomes localized than TD-SE-DD-RSH at $K-$point. Interestingly, a close resemblance between both squared amplitudes indicates the closeness of both spectra, although there is a difference of 0.4 eV in exciton binding energies. In this plot, both TDDFT and BSE spectra are produced with a very dense regular $\mathbf{k}$ grid $24 \times 24 \times 1$, and we use Gaussian broadening [128],

$$A_{e,h}^\Lambda(\mathbf{k}) = \sum_{k'} \frac{A_{e,h}^\Lambda(\mathbf{k})w_{k'}}{(\sigma\sqrt{2\pi})^3} \exp(-\frac{|\mathbf{k} - \mathbf{k}'|^2}{2\sigma^2}) \qquad (28)$$

with $w_{k'}$ being the weight and $\sigma = 0.05$ being the broadening.

Also, it is well known that the imaginary part of the dielectric response is related to the exciton amplitude via

$$\epsilon_2(\omega) \propto \sum_\Lambda \underbrace{\sum_{e,h} \left| A_{e,h}^\Lambda(\mathbf{k})\langle e|\vec{D}|h\rangle \right|^2}_{\sum_{eh} |A_{e,h}^\Lambda(\mathbf{k})|^2} \delta(E_e - E_h - \omega) \ , (29)$$

where $\vec{D}$ is the transition dipole moment.

D. MoS$_2$/WS$_2$ heterostructure

To rigorously evaluate the transferability and predictive accuracy of the screened-exchange dielectric-dependent range-separated hybrid (SE-DD-RSH) functional, we extend its application to the MoS$_2$/WS$_2$ heterostructure in the AA' stacking configuration, focusing on the electronic band structure, optical absorption spectra, and excitonic states. The atomic structure of the heterobilayer is adopted from the optimized configuration reported in Ref. [130], with the in-plane lattice parameter constrained to the experimental bulk value of 3.162 Å.

The band structures computed using G_0W_0@PBE and SE-DD-RSH are presented in Fig. 6, along with the optical absorption spectra obtained from BSE@G_0W_0 and TD-SE-DD-RSH. Notably, spin-orbit coupling (SOC) effects are neglected in these calculations, following the discussions in Ref. [130]. The direct quasiparticle band gap at the K point, as obtained from G_0W_0, is 2.33 eV, serving as a reference for benchmarking the performance of hybrid functionals.

The SE-DD-RSH calculations, we employ $[\epsilon_\infty^{2D}]^{-1} = 0.1180$ and $\mu_{layer} = 1.096$ Å^{-1}, ensuring consistency with the underlying dielectric environment. The out-of-plane lattice parameter ($c = 40.0$ Å) and the effective layer thickness ($t = 12.37118$ Å) are derived from structural relaxations, providing the necessary input for computing $[\epsilon_\infty^{2D}]^{-1}$. The definition of heterobilayer thickness (t) plays a crucial role in normalizing the in-plane and out-of-plane dielectric screening properties. We adopt a systematic scaling framework, wherein the thickness of the heterostructure is computed as: $t = \frac{t_{MoS_2}+t_{WS_2}}{2} + d_{interlayer}$, where, t_{MoS_2} and t_{WS_2} represent the monolayer thicknesses of MoS$_2$ and WS$_2$, respectively (as determined from their corresponding bilayer structures), while $d_{interlayer}$ denotes the equilibrium interlayer spacing in the heterobilayer configuration. This approach establishes a consistent framework for defining the hetero-bilayer thickness, providing a reliable basis for normalizing the in-plane and out-of-plane dielectric constants using the established scaling relations. On the other hand, for μ_{layer}, we consider the same formula as Eq. 17 with $N_e = 6$ (the same valance electron for Mo or W). Finally, the band gap obtained from SE-DD-RSH is 2.08 eV, in close agreement with the G_0W_0 result. In comparison, HSE06 significantly underestimates the band gap, yielding a direct transition of
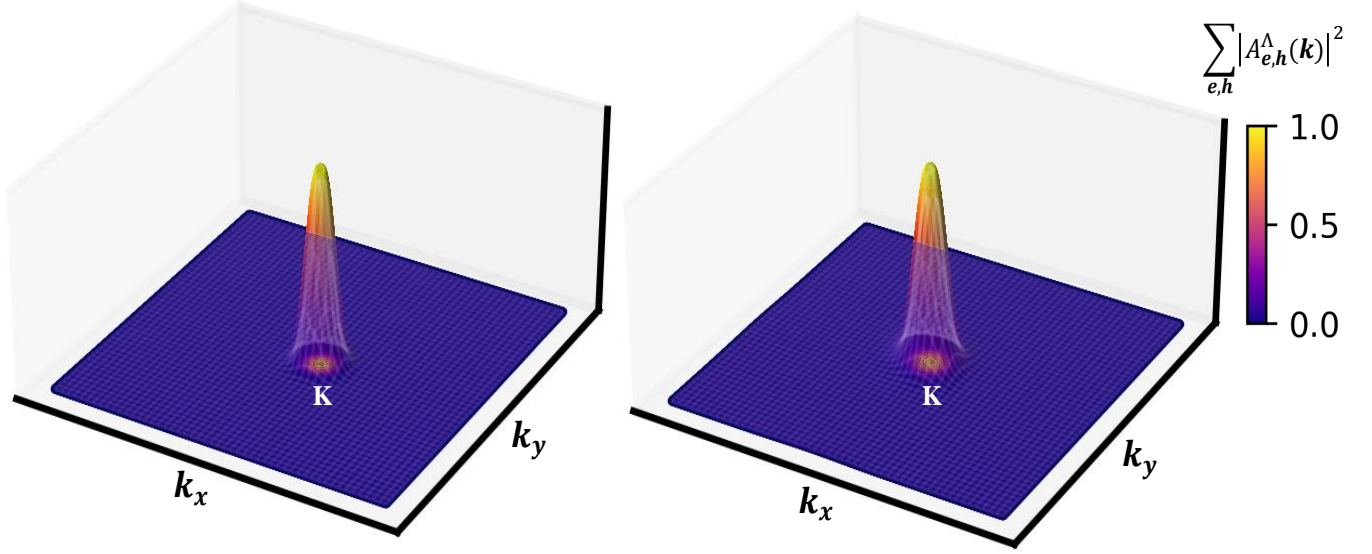
FIG. 5. Squared modulus amplitude $|A_{e,h}^{\Lambda}(\mathbf{k})|^2$ of the first bright exciton for MoS_2 monolayer along the $k_x - k_y$ plane ($k_z = 0$) in the Brillouin zone. The left panel is for BSE and the right panel is for TD-SE-DD-RSH. The eigenvectors are extracted with the $24 \times 24 \times 1$ $\mathbf{k}-$point for both calculations.

TABLE V. DFT (G_0W_0) and TDDFT (BSE) band gaps and excitonic positions of the lowest bound excitons for MoS_2/WS_2 heterostructure. Reported values are without SOC correction. All values are in eV.

MBPT			HSE06			SE-DD-RSH[a]			Expt. Peak
G_0W_0	BSE	Δ	E_g	TDDFT	Δ	E_g	TDDFT	Δ	
2.33	1.91	0.425	1.92	1.95	0.011	2.08	1.90	0.129	1.882 [129]

[a] A shift of 0.212 eV yields a TDDFT+Shift value of 1.74 eV, with the corresponding binding energy (Δ) being 0.341 eV.

1.92 eV, further reinforcing the necessity of incorporating dielectric-dependent screening in hybrid functionals.

For the optical spectra, the first bright interlayer excitation at the K point is found at 1.91 eV using BSE@G_0W_0, resulting in an exciton binding energy of 0.425 eV. In the case of TD-SE-DD-RSH, the first bright excitonic state appears at 1.90 eV, with a corresponding exciton binding energy of 0.129 eV. However, applying an empirical shift on top of TD-SE-DD-RSH shifts the first peak to 0.212 eV, corresponding to a binding energy of 0.341 eV. Overall, the results obtained from TD-SE-DD-RSH and its shifted version are quite encouraging and can be further used as benchmarks for future studies on the excitonic effects of the hetero-bilayer materials. One may note that the experimental exciton peak is obtained to be at 1.882 eV [129]. The consistency between our theo-

retical predictions and experimental findings underscores the physical robustness of the SE-DD-RSH approach in capturing excitonic effects in van der Waals heterostructures.

IV. CONCLUSIONS

The screened-exchange dielectric-dependent range-separated hybrid (SE-DD-RSH) approach presents a computationally efficient and physically robust alternative to many-body perturbation theory (GW) calculations. Unlike conventional hybrid functionals that rely on a fixed fraction of Fock exchange, SE-DD-RSH dynamically incorporates system-dependent dielectric screen-
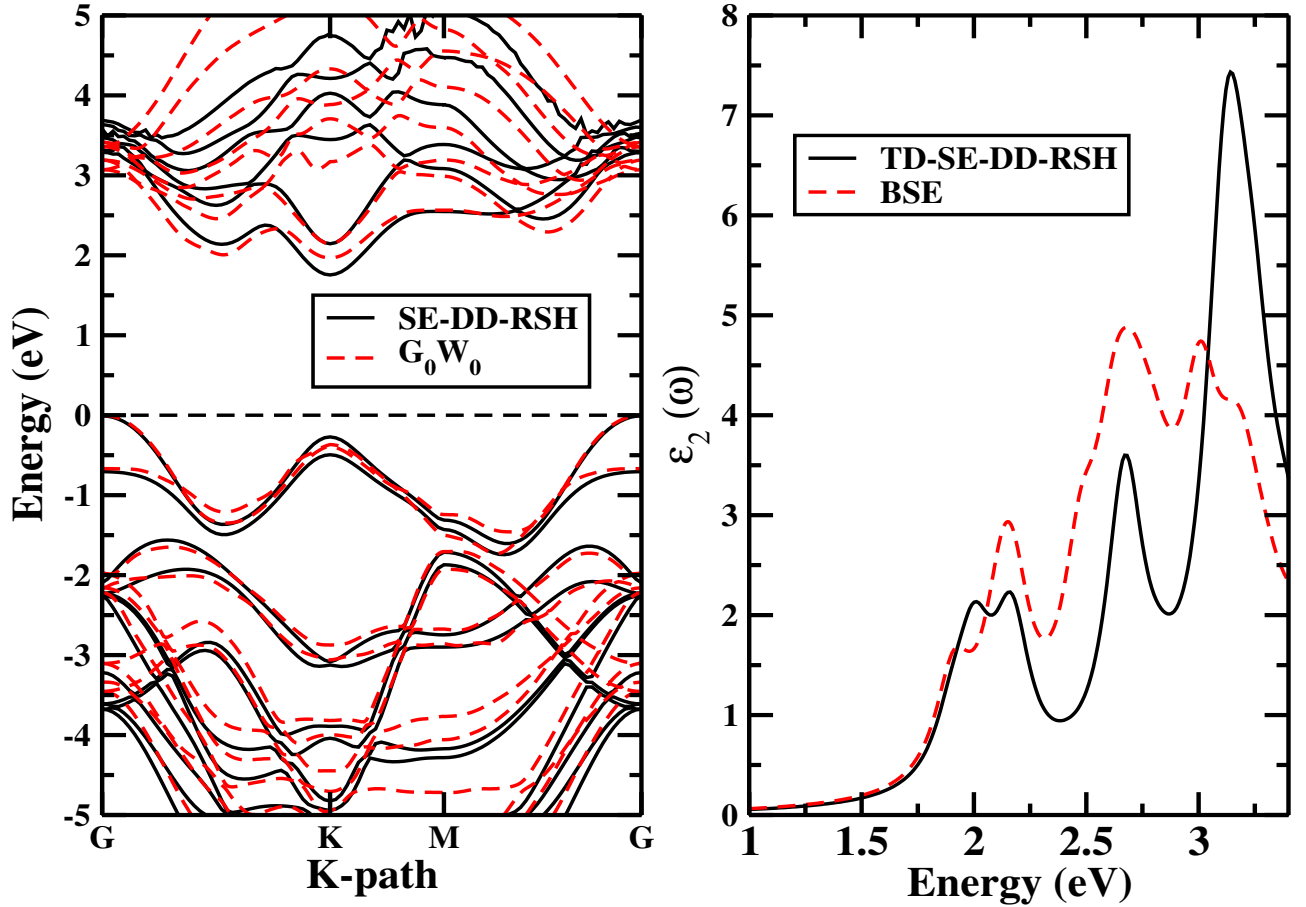
FIG. 6. Band structure and optical absorption spectra of MoS_2/WS_2 heterostructure.

ing, making it a more adaptive and physically motivated framework for electronic structure calculations.

In this work, we have developed a first-principles framework for constructing system-specific screening parameters, enabling the accurate modeling of quasiparticle band structures and optical absorption spectra in bulk, two-dimensional (2D), and heterostructured van der Waals (vdW) materials. Our TD-SE-DD-RSH formalism, applied to transition metal dichalcogenides (TMDCs), transition metal monochalcogenides (TMMCs), β-InSe, and black phosphorus (BP), demonstrates excellent agreement with G_0W_0 quasiparticle energies and BSE@G_0W_0 optical spectra, establishing its reliability in describing excitonic effects across different material classes.

A key strength of this approach is its formal consistency with dielectric-dependent hybrid (DDH) functionals developed for bulk systems, where the screening parameters are directly obtained from the dielectric response of the material. This feature makes SE-DD-RSH highly transferable, allowing it to be systematically applied to a broad range of low-dimensional quantum materials without requiring empirical tuning from higher-level methods.

Overall, the SE-DD-RSH functional and its time-dependent framework outperform HSE06 in predicting band gaps and excitonic properties. This functional can be recommended as it also employs minimal empiricism. Beyond the systems studied here, this framework can be extended to emerging research directions, including vdW spin valves[131], vdW heterostructures with moiré superlattices[4], and 2D magnetic semiconductors [132]. The ability of SE-DD-RSH to capture complex many-body interactions while maintaining computational efficiency paves the way for predictive modeling of excitonic phenomena, strongly correlated states, and next-generation optoelectronic devices in layered materials.
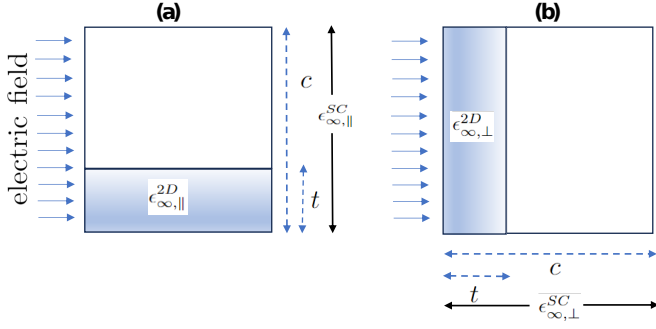
FIG. A1. Schematic diagram of two dielectric mediums (2D materials and vacuum) with the plane (a) parallel and (b) perpendicular to the applied electric field.

DATA AVAILABILITY

All data supporting this study are available within the paper. The structural files used in this work are openly accessible on Zenodo [133]. Additional data are available from the authors upon reasonable request.

Appendix A: Proof of Eq. 9 and Eq. 11

The proof of Eq. 9 is based on the concept of the two dielectric media arranged parallel and perpendicular to the applied electric field with thickness t and supercell thickness c. This is shown in Fig. A1. The thickness, t is calculated by computing $n-$ layer thickness considering the structure of $n + 1$ -layer as discussed in ref. [111].

When the two dielectric mediums, such as 2D material and vacuum, are arranged $\parallel$ to the applied electric field, the dielectric constant of the supercell (SC), consisting of the 2D material and vacuum, is given by

$$c \, \epsilon_{\infty,\parallel}^{SC} = t \, \epsilon_{\infty,\parallel}^{2D} + (c - t) \ . \tag{A1}$$

Here, we consider the dielectric constant of the vacuum to be $\epsilon_{\infty}^{vaccum} = 1$. Using Eq. A1, we readily obtain the first sets of Eq. 9, i.e.,

$$\epsilon_{\infty\parallel}^{2D} \; = \; 1 + \frac{c}{t}(\epsilon_{\infty\parallel}^{SC} - 1) \ . \tag{A2}$$

Similarly, when the dielectric mediums are arranged $\perp$ to the applied electric field, the dielectric constant of the supercell (SC), consisting of the 2D material and vacuum, is obtained as [110],

$$\frac{c}{\epsilon_{\infty,\perp}^{SC}} = \frac{t}{\epsilon_{\infty,\perp}^{2D}} + (c - t) \ . \tag{A3}$$

From Eq. A3, we obtain the second set of Eq. 9, i.e.,

$$\epsilon_{\infty\perp}^{2D} \; = \; [1 + \frac{c}{t}(\frac{1}{\epsilon_{\infty\perp}^{SC}} - 1)]^{-1} \ . \tag{A4}$$

Now in order to proof Eq. 10, i.e.,

$$\epsilon_{\infty}^{\mathrm{2D, \, eff}} = \sqrt{\epsilon_{\infty\parallel}^{2D} \cdot \epsilon_{\infty\perp}^{2D}} \ , \tag{A5}$$

we start by considering the problem from the perspective of capacitance in anisotropic media. The capacitance C of a standard parallel-plate capacitor filled with an isotropic dielectric is given by,

$$C = \epsilon \cdot \frac{A}{d} \ , \tag{A6}$$

where ϵ is the dielectric constant of the material, A is the area of the capacitor plates, and d is the distance between the plates. However, in the case of anisotropic media, the dielectric constant is different in the parallel and perpendicular directions, so we can no longer use a single ϵ value. In an anisotropic dielectric medium, the dielectric response is characterized by $\epsilon_{\infty\parallel}^{2D}$, the dielectric constant for the in-plane (parallel) direction and $\epsilon_{\infty\perp}^{2D}$, the dielectric constant for the out-of-plane (perpendicular) direction.

Let's now model this system as having two capacitances, $C_{\parallel}^{2D}$, which is associated with the dielectric response in the parallel direction and $C_{\perp}^{2D}$, which is associated with the dielectric response in the perpendicular direction. These two components will be combined to give the overall effective dielectric response.

For capacitances in series, the effective capacitance $C^{\mathrm{2D, \, eff}}$ is given by

$$\frac{1}{C^{\mathrm{2D,eff}}} = \frac{1}{C_{\parallel}^{\mathrm{2D}}} + \frac{1}{C_{\perp}^{\mathrm{2D}}} \ . \tag{A7}$$

Now, the expressions for capacitances $C_{\parallel}^{\mathrm{2D}}$ and $C_{\perp}^{\mathrm{2D}}$ can be expressed using the dielectric constants in the corresponding directions as,

$$\begin{aligned} C_{\parallel}^{\mathrm{2D}} &= \epsilon_{\infty\parallel}^{2D} \cdot \frac{A}{d} \\ C_{\perp}^{\mathrm{2D}} &= \epsilon_{\infty\perp}^{2D} \cdot \frac{A}{d} \ . \end{aligned} \tag{A8}$$

Combining the Eq. A7 and Eq. A9 into the series capacitance equation results,

$$C^{\mathrm{2D,eff}} = \frac{A}{d} \cdot \frac{1}{\frac{1}{\epsilon_{\infty\parallel}^{2D}} + \frac{1}{\epsilon_{\infty\perp}^{2D}}} \ . \tag{A9}$$

The effective dielectric constant $C^{\mathrm{2D,eff}}$ is also related to an effective dielectric constant $\epsilon_{\infty}^{\mathrm{2D, \, eff}}$, which gives the overall dielectric response of the anisotropic medium, thus,

$$C^{\mathrm{2D,eff}} = \epsilon_{\infty}^{\mathrm{2D, \, eff}} \cdot \frac{A}{d} \ . \tag{A10}$$

Equating Eq. A9 and Eq. A11 results

$$\epsilon_{\infty}^{\mathrm{2D, \, eff}} = \left(\frac{1}{\epsilon_{\infty\parallel}^{2D}} + \frac{1}{\epsilon_{\infty\perp}^{2D}} \right)^{-1} \tag{A11}$$

Now, using harmonic and geometric mean, the Eq. A11 will be further used to prove Eq. A5.

As a proof of concept, let's consider the harmonic mean $\mathcal{H}$ of two values $\mathcal{A}$ and $\mathcal{B}$ is given by

$$\mathcal{H} = \left(\frac{1}{\mathcal{A}} + \frac{1}{\mathcal{B}}\right)^{-1} = \frac{2\mathcal{A}\mathcal{B}}{\mathcal{A} + \mathcal{B}} \ . \qquad \text{(A12)}$$

The geometric mean $\mathcal{G}$ of the same two values is given by

$$\mathcal{G} = \sqrt{\mathcal{A} \cdot \mathcal{B}} \ . \qquad \text{(A13)}$$

We want to prove that for similar values of $\mathcal{A}$ and $\mathcal{B}$, the harmonic mean approaches the geometric mean, i.e.,

$$\mathcal{H} \approx \mathcal{G} \quad \text{as} \quad \mathcal{A} \approx \mathcal{B} \ . \qquad \text{(A14)}$$

let's consider $\mathcal{A}$ and $\mathcal{B}$ deviates from mean value $m (= \frac{\mathcal{A}+\mathcal{B}}{2})$ by δ_x and δ_y (where both δ_x and δ_y are small enough) i.e., $\mathcal{A} \approx m + \delta_x$ and $\mathcal{B} \approx m + \delta_y$. Thus, substituting in Eq. A12

$$\begin{aligned}
\mathcal{H} &= \frac{2(m + \delta_x)(m + \delta_y)}{(m + \delta_x) + (m + \delta_y)} \\
&\approx \frac{2(m^2 + m\delta_x + m\delta_y)}{2m + \delta_x + \delta_y} \approx m \ . \qquad \text{(A15)}
\end{aligned}$$

Now let's expand the geometric mean in terms of $\mathcal{A}$ and $\mathcal{B}$. Substituting $\mathcal{A} \approx m + \delta_x$ and $\mathcal{B} \approx m + \delta_y$ in

Eq. A13 results,

$$\begin{aligned}
\mathcal{G} &= \sqrt{(m + \delta_x)(m + \delta_y)} \\
&= \sqrt{m^2 + m\delta_x + m\delta_y + \delta_x\delta_y} \\
&\approx \sqrt{m^2 + m\delta_x + m\delta_y} \\
&\approx m\sqrt{1 + \frac{\delta_x + \delta_y}{m}} \ . \qquad \text{(A16)}
\end{aligned}$$

For small $\frac{\delta_x + \delta_y}{m}$, we can approximate the square root using a binomial expansion:

$$\mathcal{G} \approx m\left(1 + \frac{\delta_x + \delta_y}{2m}\right) \approx m \ . \qquad \text{(A17)}$$

The harmonic mean $\mathcal{H}$ and the geometric mean $\mathcal{G}$ reduce to approximately m when x and y are close. Therefore, as x and y approach each other, and the harmonic mean approaches the geometric mean, i.e.,

$$H \approx G \qquad \text{(A18)}$$

This justifies the proof of Eq. A5 via Eq. A11, i.e.,

$$\epsilon_\infty^{\text{2D, eff}} = \left(\frac{1}{\epsilon_{\infty\parallel}^{2D}} + \frac{1}{\epsilon_{\infty\perp}^{2D}}\right)^{-1} \approx \sqrt{\epsilon_{\infty\parallel}^{2D} \cdot \epsilon_{\infty\perp}^{2D}} \qquad \text{(A19)}$$

Appendix B: Details of the Material Parameters Used in This Study

TABLE VI: In-plane (a) and out-of-plane (b) lattice constants (in Å) are provided. The c values for the bulk structure are also given with $c = t$ (in Å). In-plane and out-of-plane dielectric properties are included as well.

System	Layer	a	b	c	t	$\epsilon_{\infty,\parallel}^{SC}$	$\epsilon_{\infty,\perp}^{SC}$	$\epsilon_{\infty\parallel}^{2D}$	$\epsilon_{\infty\perp}^{2D}$
MoS$_2$	Bulk	3.147	3.147	12.305	—	14.173	6.241	—	—
	1L	3.150	3.150	35.0	6.062	3.272	1.164	14.117	5.409
	2L	3.150	3.150	40.0	12.111	5.031	1.337	14.314	6.028
MoSe$_2$	Bulk	3.273	3.273	12.892	—	15.738	7.995	—	—
	1L	3.263	3.263	35.0	6.384	3.643	1.182	15.494	6.511
	2L	3.258	3.258	40.0	12.762	5.684	1.380	15.682	7.371
MoTe$_2$	Bulk	3.494	3.494	13.901	—	18.978	11.024	—	—
	1L	3.488	3.488	35.0	6.847	4.464	1.210	18.707	9.060
	2L	3.483	3.483	45.0	13.688	6.488	1.379	19.042	10.500
WS$_2$	Bulk	3.147	3.147	12.367	—	12.955	5.795	—	—
	1L	3.133	3.133	35.0	6.077	3.058	1.164	12.855	5.352
	2L	3.128	3.128	40.0	12.156	4.646	1.335	12.998	5.783
WSe$_2$	Bulk	3.282	3.282	12.960	—	14.499	8.360	—	—
	1L	3.267	3.267	35.0	6.415	3.422	1.182	14.215	6.353
	2L	3.262	3.262	45.0	12.817	4.812	1.323	14.383	7.008

WTe$_2$	Bulk	3.494	3.494	13.971	—	18.083	12.616	—	—
	1L	3.499	3.499	35.0	6.871	4.273	1.210	17.677	8.831
	2L	3.491	3.491	45.0	13.715	6.177	1.378	17.988	10.128
hBN	Bulk	2.507	2.507	6.578	—	4.569	2.573	—	—
	1L	2.494	2.494	30.0	3.317	1.394	1.068	4.569	2.363
	2L	2.492	2.492	35.0	6.634	1.673	1.125	4.551	2.440
InSe	Bulk	4.034	4.034	16.840	—	7.457	11.477	—	—
	1L	4.034	4.034	20.0	8.416	3.620	1.542	7.225	6.096
	2L	4.043	4.043	30.0	16.808	4.550	1.915	7.336	6.801
BP	Bulk	3.313	4.496	10.986	—	10.909	5.843	—	—
	1L	3.305	4.434	20.0	5.318	5.064	1.279	16.282	5.617
	2L	3.305	4.434	26.0	10.637	10.77	1.536	24.881	6.827
MoS$_2$/WS$_2$	Heterostrcuture	3.190	3.190	40.0	12.371	4.926	1.333	13.695	5.241

[1] A. K. Geim and K. S. Novoselov, The rise of graphene, Nature Materials **6**, 183 (2007).

[2] A. Gupta, T. Sakthivel, and S. Seal, Recent development in 2d materials beyond graphene, Progress in Materials Science **73**, 44 (2015).

[3] Q. H. Wang, K. Kalantar-Zadeh, A. Kis, J. N. Coleman, and M. S. Strano, Electronics and optoelectronics of two-dimensional transition metal dichalcogenides, Nature Nanotechnology **7**, 699 (2012).

[4] A. K. Geim and I. V. Grigorieva, Van der waals heterostructures, Nature **499**, 419 (2013).

[5] K. S. Novoselov, A. Mishchenko, A. Carvalho, and A. H. C. Neto, 2d materials and van der waals heterostructures, Science **353**, aac9439 (2016), https://www.science.org/doi/pdf/10.1126/science.aac9439.

[6] P. Ajayan, P. Kim, and K. Banerjee, Two-dimensional van der Waals materials, Physics Today **69**, 38 (2016), https://pubs.aip.org/physicstoday/article-pdf/69/9/38/10117753/38_1_online.pdf.

[7] W. Choi, N. Choudhary, G. H. Han, J. Park, D. Akinwande, and Y. H. Lee, Recent development of two-dimensional transition metal dichalcogenides and their applications, Materials Today **20**, 116 (2017).

[8] S. Manzeli, D. Ovchinnikov, D. Pasquier, O. V. Yazyev, and A. Kis, 2d transition metal dichalcogenides, Nature Reviews Materials **2**, 17033 (2017).

[9] A. V. Kolobov and J. Tominaga, *Two-Dimensional Transition-Metal Dichalcogenides*, Vol. 239 (2016).

[10] K. F. Mak, C. Lee, J. Hone, J. Shan, and T. F. Heinz, Atomically thin mos$_2$: A new direct-gap semiconductor, Phys. Rev. Lett. **105**, 136805 (2010).

[11] A. Splendiani, L. Sun, Y. Zhang, T. Li, J. Kim, C.-Y. Chim, G. Galli, and F. Wang, Emerging photoluminescence in monolayer mos2, Nano Letters **10**, 1271 (2010), pMID: 20229981, https://doi.org/10.1021/nl903868w.

[12] K. Kaasbjerg, K. S. Thygesen, and K. W. Jacobsen, Phonon-limited mobility in n-type single-layer mos$_2$ from first principles, Phys. Rev. B **85**, 115317 (2012).

[13] F. A. Rasmussen and K. S. Thygesen, Computational 2d materials database: Electronic structure of transition-metal dichalcogenides and oxides, The Journal of Physical Chemistry C **119**, 13169 (2015), https://doi.org/10.1021/acs.jpcc.5b02950.

[14] S. Haastrup, M. Strange, M. Pandey, T. Deilmann, P. S. Schmidt, N. F. Hinsche, M. N. Gjerding, D. Torelli, P. M. Larsen, A. C. Riis-Jensen, J. Gath, K. W. Jacobsen, J. J. Mortensen, T. Olsen, and K. S. Thygesen, The computational 2d materials database: high-throughput modeling and discovery of atomically thin crystals, 2D Materials **5**, 042002 (2018).

[15] K. Andersen, S. Latini, and K. S. Thygesen, Dielectric genome of van der waals heterostructures, Nano Letters **15**, 4616 (2015), pMID: 26047386, https://doi.org/10.1021/acs.nanolett.5b01251.

[16] M. Massicotte, F. Vialla, P. Schmidt, M. B. Lundeberg, S. Latini, S. Haastrup, M. Danovich, D. Davydovskaya, K. Watanabe, T. Taniguchi, V. I. Fal'ko, K. S. Thygesen, T. G. Pedersen, and F. H. L. Koppens, Dissociation of two-dimensional excitons in monolayer wse2, Nature Communications **9**, 1633 (2018).

[17] S. Gupta, J.-J. Zhang, J. Lei, H. Yu, M. Liu, X. Zou, and B. I. Yakobson, Two-dimensional transition metal dichalcogenides: A theory and simulation perspective, Chemical Reviews **125**, 786 (2025), pMID: 39746214, https://doi.org/10.1021/acs.chemrev.4c00628.

[18] Y. Liu, N. O. Weiss, X. Duan, H.-C. Cheng, Y. Huang, and X. Duan, Van der waals heterostructures and devices, Nature Reviews Materials **1**, 16042 (2016).

[19] L. Balents, C. R. Dean, D. K. Efetov, and A. F. Young, Superconductivity and strong correlations in moiré flat bands, Nature Physics **16**, 725 (2020).

[20] E. Y. Andrei, D. K. Efetov, P. Jarillo-Herrero, A. H. MacDonald, K. F. Mak, T. Senthil, E. Tutuc, A. Yazdani, and A. F. Young, The marvels of moiré materials, Nature Reviews Materials **6**, 201 (2021).

[21] A. Castellanos-Gomez, X. Duan, Z. Fei, H. R. Gutierrez,

Y. Huang, X. Huang, J. Quereda, Q. Qian, E. Sutter, and P. Sutter, Van der waals heterostructures, Nature Reviews Methods Primers **2**, 58 (2022).

[22] M. V. Stern, Y. Waschitz, W. Cao, I. Nevo, K. Watanabe, T. Taniguchi, E. Sela, M. Urbakh, O. Hod, and M. B. Shalom, Interfacial ferroelectricity by van der waals sliding, Science **372**, 1462 (2021), https://www.science.org/doi/pdf/10.1126/science.abe8177.

[23] Y. Zhang, T.-R. Chang, B. Zhou, Y.-T. Cui, H. Yan, Z. Liu, F. Schmitt, J. Lee, R. Moore, Y. Chen, H. Lin, H.-T. Jeng, S.-K. Mo, Z. Hussain, A. Bansil, and Z.-X. Shen, Direct observation of the transition from indirect to direct bandgap in atomically thin epitaxial mose2, Nature Nanotechnology **9**, 111 (2014).

[24] J. Kang, S. Tongay, J. Zhou, J. Li, and J. Wu, Band offsets and heterostructures of two-dimensional semiconductors, Applied Physics Letters **102**, 012111 (2013), https://pubs.aip.org/aip/apl/article-pdf/doi/10.1063/1.4774090/14263519/012111_1_online.pdf.

[25] C. Gong, H. Zhang, W. Wang, L. Colombo, R. M. Wallace, and K. Cho, Band alignment of two-dimensional transition metal dichalcogenides: Application in tunnel field effect transistors, Applied Physics Letters **103**, 053513 (2013), https://pubs.aip.org/aip/apl/article-pdf/doi/10.1063/1.4817409/14296538/053513_1_online.pdf.

[26] Z. Y. Zhu, Y. C. Cheng, and U. Schwingenschlögl, Giant spin-orbit-induced spin splitting in two-dimensional transition-metal dichalcogenide semiconductors, Phys. Rev. B **84**, 153402 (2011).

[27] G.-B. Liu, W.-Y. Shan, Y. Yao, W. Yao, and D. Xiao, Three-band tight-binding model for monolayers of group-vib transition metal dichalcogenides, Phys. Rev. B **88**, 085433 (2013).

[28] H.-g. Kim and H. J. Choi, Thickness dependence of work function, ionization energy, and electron affinity of mo and w dichalcogenides from dft and gw calculations, Phys. Rev. B **103**, 085404 (2021).

[29] F. Tran, J. Doumont, L. Kalantari, P. Blaha, T. Rauch, P. Borlido, S. Botti, M. A. L. Marques, A. Patra, S. Jana, and P. Samal, Bandgap of two-dimensional materials: Thorough assessment of modern exchange–correlation functionals, The Journal of Chemical Physics **155**, 104103 (2021).

[30] A. Patra, S. Jana, P. Samal, F. Tran, L. Kalantari, J. Doumont, and P. Blaha, Efficient band structure calculation of two-dimensional materials from semilocal density functionals, The Journal of Physical Chemistry C **125**, 11206 (2021), pMID: 34084266, https://doi.org/10.1021/acs.jpcc.1c02031.

[31] A. Patra, B. Patra, L. A. Constantin, and P. Samal, Electronic band structure of layers within meta generalized gradient approximation of density functionals, Phys. Rev. B **102**, 045135 (2020).

[32] P. Borlido, J. Schmidt, A. W. Huran, F. Tran, M. A. L. Marques, and S. Botti, Exchange-correlation functionals for band gaps of solids: benchmark, reparametrization and machine learning, npj Computational Materials **6**, 96 (2020).

[33] F. Tran and P. Blaha, Importance of the kinetic energy density for band gap calculations in solids with density functional theory, The Journal of Physical Chemistry A **121**, 3318 (2017), pMID: 28402113, https://doi.org/10.1021/acs.jpca.7b02882.

[34] B. Patra, S. Jana, L. A. Constantin, and P. Samal, Ef-

[35] A. Ghosh, S. Jana, T. Rauch, F. Tran, M. A. L. Marques, S. Botti, L. A. Constantin, M. K. Niranjan, and P. Samal, Efficient and improved prediction of the band offsets at semiconductor heterojunctions from meta-gga density functionals: A benchmark study, The Journal of Chemical Physics **157**, 124108 (2022).

[36] Y. Rui, Y. Chen, E. Ivanova, V. B. Kumar, S. Śmiga, I. Grabowski, and P. O. Dral, The best dft functional is the ensemble of functionals, Advanced Science **11**, 2408239 (2024).

[37] V. B. Kumar, S. Śmiga, and I. Grabowski, A critical evaluation of the hybrid ks dft functionals based on the ks exchange-correlation potentials, The Journal of Physical Chemistry Letters **15**, 10219 (2024), pMID: 39356205, https://doi.org/10.1021/acs.jpclett.4c01979.

[38] S. Jana, A. Patra, and P. Samal, Assessing the performance of the Tao-Mo semilocal density functional in the projector-augmented-wave method, The Journal of Chemical Physics **149**, 044120 (2018), https://pubs.aip.org/aip/jcp/article-pdf/doi/10.1063/1.5040786/14927796/044120_1_online.pdf.

[39] B. Patra, S. Jana, L. A. Constantin, and P. Samal, Relevance of the pauli kinetic energy density for semilocal functionals, Phys. Rev. B **100**, 155140 (2019).

[40] J. Sun, A. Ruzsinszky, and J. P. Perdew, Strongly constrained and appropriately normed semilocal density functional, Phys. Rev. Lett. **115**, 036402 (2015).

[41] S. Jana, S. K. Behera, S. Śmiga, L. A. Constantin, and P. Samal, Improving the applicability of the pauli kinetic energy density based semilocal functional for solids, New J. Phys. **23**, 063007 (2021).

[42] S. Jana, K. Sharma, and P. Samal, Improving the performance of tao–mo non-empirical density functional with broader applicability in quantum chemistry and materials science, The Journal of Physical Chemistry A **123**, 6356 (2019).

[43] A. Patra, S. Jana, and P. Samal, A way of resolving the order-of-limit problem of tao–mo semilocal functional, The Journal of Chemical Physics **153**, 184112 (2020).

[44] S. Jana, S. K. Behera, S. Śmiga, L. A. Constantin, and P. Samal, Accurate density functional made more versatile, The Journal of Chemical Physics **155**, 024103 (2021).

[45] T. Lebeda, T. Aschebrock, and S. Kümmel, Balancing the contributions to the gradient expansion: Accurate binding and band gaps with a nonempirical meta-gga, Phys. Rev. Lett. **133**, 136402 (2024).

[46] B. Neupane, H. Tang, N. K. Nepal, S. Adhikari, and A. Ruzsinszky, Opening band gaps of low-dimensional materials at the meta-gga level of density functional approximations, Phys. Rev. Mater. **5**, 063803 (2021).

[47] T. Lebeda, T. Aschebrock, J. Sun, L. Leppert, and S. Kümmel, Right band gaps for the right reason at low computational cost with a meta-gga, Phys. Rev. Mater. **7**, 093803 (2023).

[48] S. Jana, B. Patra, S. Smiga, L. A. Constantin, and P. Samal, Improved solid stability from a screened range-separated hybrid functional by satisfying semiclassical atom theory and local density linear response, Phys. Rev. B **102**, 155107 (2020).

[49] S. Jana, L. A. Constantin, S. Śmiga, and P. Samal,

Solid-state performance of a meta-gga screened hybrid density functional constructed from pauli kinetic enhancement factor dependent semilocal exchange hole, The Journal of Chemical Physics **157**, 024102 (2022).

[50] S. Jana and P. Samal, A meta-gga level screened range-separated hybrid functional by employing short range hartree-fock with a long range semilocal functional, Phys. Chem. Chem. Phys. **20**, 8999 (2018).

[51] S. Jana and P. Samal, Screened hybrid meta-gga exchange–correlation functionals for extended systems, Phys. Chem. Chem. Phys. **21**, 3002 (2019).

[52] S. Jana, A. Patra, and P. Samal, Efficient lattice constants and energy bandgaps for condensed systems from a meta-GGA level screened range-separated hybrid functional, The Journal of Chemical Physics **149**, 094105 (2018), https://pubs.aip.org/aip/jcp/article-pdf/doi/10.1063/1.5037030/13632513/094105_1_online.pdf.

[53] S. Jana, A. Patra, L. A. Constantin, and P. Samal, Screened range-separated hybrid by balancing the compact and slowly varying density regimes: Satisfaction of local density linear response, J. Chem. Phys. **152**, 044111 (2020).

[54] X. Wang, M. Dvorak, and Z. Wu, Hybrid functionals with fixed mixing parameter perform no better than pbe for fundamental band gaps of nanoscale materials, Phys. Rev. B **94**, 195429 (2016).

[55] L. Hedin, New method for calculating the one-particle green's function with application to the electron-gas problem, Phys. Rev. **139**, A796 (1965).

[56] L. Hedin and S. Lundqvist, Effects of electron-electron and electron-phonon interactions on the one-electron states of solids (Academic Press, 1970) pp. 1–181.

[57] G. Onida, L. Reining, and A. Rubio, Electronic excitations: density-functional versus many-body green's-function approaches, Rev. Mod. Phys. **74**, 601 (2002).

[58] M. Hossain and J. Bhattacharjee, *Self energy corrected tight-binding framework in directed hybrid orbital basis from first principles*, Ph.D. thesis, School of Physical Sciences, NISER, Bhubaneswar (2022).

[59] W. Gao, W. Xia, P. Zhang, J. R. Chelikowsky, and J. Zhao, Numerical methods for efficient gw calculations and the applications in low-dimensional systems, Electronic Structure **4**, 023003 (2022).

[60] M. Hossain, J. De, and J. Bhattacharjee, Hybrid atomic orbital basis from first principles: Bottom-up mapping of self-energy correction to large covalent systems, The Journal of Physical Chemistry A **125**, 6805 (2021).

[61] M. Drüppel, T. Deilmann, J. Noky, P. Marauhn, P. Krüger, and M. Rohlfing, Electronic excitations in transition metal dichalcogenide monolayers from an LDA$+GdW$ approach, Phys. Rev. B **98**, 155433 (2018).

[62] C. Espejo, T. Rangel, A. H. Romero, X. Gonze, and G.-M. Rignanese, Band structure tunability in mos_2 under interlayer compression: A dft and GW study, Phys. Rev. B **87**, 245114 (2013).

[63] D. Y. Qiu, F. H. da Jornada, and S. G. Louie, Optical spectrum of mos_2: Many-body effects and diversity of exciton states, Phys. Rev. Lett. **111**, 216805 (2013).

[64] L. Yang, C.-H. Park, Y.-W. Son, M. L. Cohen, and S. G. Louie, Quasiparticle energies and band gaps in graphene nanoribbons, Phys. Rev. Lett. **99**, 186801 (2007).

[65] X. Blase, A. Rubio, S. G. Louie, and M. L. Cohen, Quasiparticle band structure of bulk hexagonal boron nitride and related systems, Phys. Rev. B **51**, 6868 (1995).

[66] M. Hossain and J. Bhattacharjee, Transferability of self-energy correction in tight-binding basis constructed from first principles, The Journal of Chemical Physics **153** (2020).

[67] D. Y. Qiu, F. H. da Jornada, and S. G. Louie, Screening and many-body effects in two-dimensional crystals: Monolayer mos_2, Phys. Rev. B **93**, 235435 (2016).

[68] T. Cheiwchanchamnangij and W. R. L. Lambrecht, Quasiparticle band structure calculation of monolayer, bilayer, and bulk mos_2, Phys. Rev. B **85**, 205302 (2012).

[69] D. Golze, M. Dvorak, and P. Rinke, The gw compendium: A practical guide to theoretical photoemission spectroscopy, Frontiers in Chemistry **7**, 10.3389/fchem.2019.00377 (2019).

[70] G. Strinati, H. J. Mattausch, and W. Hanke, Dynamical correlation effects on the quasiparticle bloch states of a covalent crystal, Phys. Rev. Lett. **45**, 290 (1980).

[71] G. Strinati, H. J. Mattausch, and W. Hanke, Dynamical aspects of correlation corrections in a covalent crystal, Phys. Rev. B **25**, 2867 (1982).

[72] A. Ramasubramaniam, D. Wing, and L. Kronik, Transferable screened range-separated hybrids for layered materials: The cases of mos_2 and h-bn, Phys. Rev. Mater. **3**, 084007 (2019).

[73] H. Mishra, A. Bose, A. Dhar, and S. Bhattacharya, Exciton-phonon coupling and band-gap renormalization in monolayer wse_2, Phys. Rev. B **98**, 045143 (2018).

[74] M. Camarasa-Gómez, A. Ramasubramaniam, J. B. Neaton, and L. Kronik, Transferable screened range-separated hybrid functionals for electronic and optical properties of van der waals materials, Phys. Rev. Mater. **7**, 104001 (2023).

[75] M. Marsili, A. Molina-Sánchez, M. Palummo, D. Sangalli, and A. Marini, Spinorial formulation of the gw-bse equations and spin properties of excitons in two-dimensional transition metal dichalcogenides, Phys. Rev. B **103**, 155152 (2021).

[76] J. De, M. Hossain, and J. Bhattacharjee, Optical excitation from anti-causally corrected real-time dynamics in a minimal basis, arXiv preprint arXiv:2306.06701 (2023).

[77] K. W. Lau, C. Cocchi, and C. Draxl, Electronic and optical excitations of two-dimensional zrs_2 and hfs_2 and their heterostructure, Phys. Rev. Mater. **3**, 074001 (2019).

[78] C. Attaccalite, M. Grüning, and A. Marini, Real-time approach to the optical properties of solids and nanostructures: Time-dependent bethe-salpeter equation, Phys. Rev. B **84**, 245110 (2011).

[79] F. Bruneval and M. A. L. Marques, Benchmarking the starting points of the gw approximation for molecules, Journal of Chemical Theory and Computation **9**, 324 (2013), pMID: 26589035, https://doi.org/10.1021/ct300835h.

[80] S. E. Gant, J. B. Haber, M. R. Filip, F. Sagredo, D. Wing, G. Ohad, L. Kronik, and J. B. Neaton, Optimally tuned starting point for single-shot gw calculations of solids, Phys. Rev. Mater. **6**, 053802 (2022).

[81] S. Jana, A. Ghosh, A. Bhattacharjee, D. Rani, M. Hossain, and P. Samal, Nonempirical dielectric dependent hybrid as an accurate starting point for the single shot g0w0 calculation of chalcopyrite semiconductors, The Journal of Chemical Physics **162** (2025).

[82] J. Zhan, M. Govoni, and G. Galli, Nonempirical range-separated hybrid functional with spatially dependent screened exchange, Journal of Chemical Theory and Computation **19**, 5851 (2023), pMID: 37591004, https://doi.org/10.1021/acs.jctc.3c00580.

[83] S. Jana, A. Ghosh, L. A. Constantin, and P. Samal, Simple and effective screening parameter for range-separated dielectric-dependent hybrids, Phys. Rev. B **108**, 045101 (2023).

[84] A. Ghosh, S. Jana, D. Rani, M. Hossain, M. K. Niranjan, and P. Samal, Accurate and efficient prediction of the band gaps and optical spectra of chalcopyrite semiconductors from a nonempirical range-separated dielectric-dependent hybrid: Comparison with many-body perturbation theory, Phys. Rev. B **109**, 045133 (2024).

[85] D. Rani, S. Jana, M. K. Niranjan, and P. Samal, Thermoelectric characteristics of silver-based chalcopyrite semiconductors: An ab initio study based on the nonempirical range-separated dielectric-dependent hybrid, The Journal of Physical Chemistry C **0**, null (0), https://doi.org/10.1021/acs.jpcc.4c07037.

[86] W. Chen, G. Miceli, G.-M. Rignanese, and A. Pasquarello, Nonempirical dielectric-dependent hybrid functional with range separation for semiconductors and insulators, Phys. Rev. Mater. **2**, 073803 (2018).

[87] D. Wing, J. B. Haber, R. Noff, B. Barker, D. A. Egger, A. Ramasubramaniam, S. G. Louie, J. B. Neaton, and L. Kronik, Comparing time-dependent density functional theory with many-body perturbation theory for semiconductors: Screened range-separated hybrids and the gw plus bethe-salpeter approach, Phys. Rev. Materials **3**, 064603 (2019).

[88] G. Ohad, D. Wing, S. E. Gant, A. V. Cohen, J. B. Haber, F. Sagredo, M. R. Filip, J. B. Neaton, and L. Kronik, Band gaps of halide perovskites from a wannier-localized optimally tuned screened range-separated hybrid functional, Phys. Rev. Mater. **6**, 104606 (2022).

[89] D. Wing, J. B. Haber, R. Noff, B. Barker, D. A. Egger, A. Ramasubramaniam, S. G. Louie, J. B. Neaton, and L. Kronik, Comparing time-dependent density functional theory with many-body perturbation theory for semiconductors: Screened range-separated hybrids and the gw plus bethe-salpeter approach, Phys. Rev. Mater. **3**, 064603 (2019).

[90] S. Jana, A. Bhattacharjee, S. Mahakal, S. Śmiga, and P. Samal, Meta-gga dielectric-dependent and range-separated screened hybrid functional for reliable prediction of material properties, Phys. Rev. B **111**, 115125 (2025).

[91] M. Gerosa, C. E. Bottani, L. Caramella, G. Onida, C. Di Valentin, and G. Pacchioni, Defect calculations in semiconductors through a dielectric-dependent hybrid dft functional: The case of oxygen vacancies in metal oxides, The Journal of Chemical Physics **143**, 134702 (2015).

[92] M. Gerosa, C. E. Bottani, L. Caramella, G. Onida, C. Di Valentin, and G. Pacchioni, Electronic structure and phase stability of oxide semiconductors: Performance of dielectric-dependent hybrid functional dft, benchmarked against gw band structure calculations and experiments, Phys. Rev. B **91**, 155201 (2015).

[93] G. Miceli, W. Chen, I. Reshetnyak, and A. Pasquarello, Nonempirical hybrid functionals for band gaps and polaronic distortions in solids, Phys. Rev. B **97**, 121112 (2018).

[94] H. Zheng, M. Govoni, and G. Galli, Dielectric-dependent hybrid functionals for heterogeneous materials, Phys. Rev. Mater. **3**, 073803 (2019).

[95] M. Gerosa, C. E. Bottani, C. D. Valentin, G. Onida, and G. Pacchioni, Accuracy of dielectric-dependent hybrid functionals in the prediction of optoelectronic properties of metal oxide semiconductors: a comprehensive comparison with many-body gw and experiments, Journal of Physics: Condensed Matter **30**, 044003 (2017).

[96] Y. Hinuma, Y. Kumagai, I. Tanaka, and F. Oba, Band alignment of semiconductors and insulators using dielectric-dependent hybrid functionals: Toward high-throughput evaluation, Phys. Rev. B **95**, 075302 (2017).

[97] N. P. Brawand, M. Govoni, M. Vörös, and G. Galli, Performance and self-consistency of the generalized dielectric dependent hybrid functional, Journal of Chemical Theory and Computation **13**, 3318 (2017).

[98] P. Liu, C. Franchini, M. Marsman, and G. Kresse, Assessing model-dielectric-dependent hybrid functionals on the antiferromagnetic transition-metal monoxides mno, feo, coo, and nio, Journal of Physics: Condensed Matter **32**, 015502 (2019).

[99] L. Kronik and S. Kümmel, Dielectric screening meets optimally tuned density functionals, Advanced Materials **30**, 1706560 (2018).

[100] A. Ramasubramaniam, D. Wing, and L. Kronik, Transferable screened range-separated hybrids for layered materials: The cases of mos$_2$ and h-bn, Phys. Rev. Materials **3**, 084007 (2019).

[101] J. P. Perdew, K. Burke, and M. Ernzerhof, Generalized gradient approximation made simple, Phys. Rev. Lett. **77**, 3865 (1996).

[102] J. Heyd, G. E. Scuseria, and M. Ernzerhof, Hybrid functionals based on a screened coulomb potential, J. Chem. Phys. **118**, 8207 (2003).

[103] J. Heyd and G. E. Scuseria, Efficient hybrid density functional calculations in solids: Assessment of the heyd–scuseria–ernzerhof screened coulomb hybrid functional, J. Chem. Phys. **121**, 1187 (2004).

[104] S. Jana and P. Samal, A meta-gga level screened range-separated hybrid functional by employing short range hartree–fock with a long range semilocal functional, Phys. Chem. Chem. Phys. **20**, 8999 (2018).

[105] A. Tal, P. Liu, G. Kresse, and A. Pasquarello, Accurate optical spectra through time-dependent density functional theory based on screening-dependent hybrid functionals, Phys. Rev. Res. **2**, 032019 (2020).

[106] M. Gajdoš, K. Hummer, G. Kresse, J. Furthmüller, and F. Bechstedt, Linear optical properties in the projector-augmented wave methodology, Phys. Rev. B **73**, 045112 (2006).

[107] R. W. Nunes and X. Gonze, Berry-phase treatment of the homogeneous electric field perturbation in insulators, Phys. Rev. B **63**, 155107 (2001).

[108] I. Souza, J. Íñiguez, and D. Vanderbilt, First-principles approach to insulators in finite electric fields, Phys. Rev. Lett. **89**, 117602 (2002).

[109] S. Baroni, S. de Gironcoli, A. Dal Corso, and P. Giannozzi, Phonons and related crystal properties from density-functional perturbation theory, Rev. Mod.

Phys. **73**, 515 (2001).

[110] D. E. Aspnes, Local-field effects and effective-medium theory: A microscopic perspective, American Journal of Physics **50**, 704 (1982), https://pubs.aip.org/aapt/ajp/article-pdf/50/8/704/12175143/704_1_online.pdf.

[111] A. Laturia, M. L. Van de Put, and W. G. Vandenberghe, Dielectric properties of hexagonal boron nitride and transition metal dichalcogenides: from monolayer to bulk, npj 2D Materials and Applications **2**, 6 (2018).

[112] D. Van Tuan, M. Yang, and H. Dery, Coulomb interaction in monolayer transition-metal dichalcogenides, Phys. Rev. B **98**, 125308 (2018).

[113] F. Hüser, T. Olsen, and K. S. Thygesen, How dielectric screening in two-dimensional crystals affects the convergence of excited-state calculations: Monolayer mos_2, Phys. Rev. B **88**, 245309 (2013).

[114] M. Camarasa-Gómez, S. E. Gant, G. Ohad, J. B. Neaton, A. Ramasubramaniam, and L. Kronik, Excitations in layered materials from a non-empirical wannier-localized optimally-tuned screened range-separated hybrid functional, npj Computational Materials **10**, 288 (2024).

[115] X. Ling, H. Wang, S. Huang, F. Xia, and M. S. Dresselhaus, The renaissance of black phosphorus, Proceedings of the National Academy of Sciences **112**, 4523 (2015), https://www.pnas.org/doi/pdf/10.1073/pnas.1416581112.

[116] V. Tran, R. Soklaski, Y. Liang, and L. Yang, Layer-controlled band gap and anisotropic excitons in few-layer black phosphorus, Phys. Rev. B **89**, 235319 (2014).

[117] G. Kresse and J. Hafner, Ab initio molecular dynamics for liquid metals, Phys. Rev. B **47**, 558 (1993).

[118] G. Kresse and J. Furthmüller, Efficient iterative schemes for ab initio total-energy calculations using a plane-wave basis set, Phys. Rev. B **54**, 11169 (1996).

[119] G. Kresse and D. Joubert, From ultrasoft pseudopotentials to the projector augmented-wave method, Phys. Rev. B **59**, 1758 (1999).

[120] G. Kresse and J. Furthmüller, Efficiency of ab-initio total energy calculations for metals and semiconductors using a plane-wave basis set, Comput. Mater. Sci. **6**, 15 (1996).

[121] M. Camarasa-Gómez, S. E. Gant, G. Ohad, J. B. Neaton, A. Ramasubramaniam, and L. Kronik, Excitations in layered materials from a non-empirical wannier-localized optimally-tuned screened range-separated hybrid functional, npj Computational Materials **10**, 288 (2024).

[122] Y. Guo and J. Robertson, Band structure, band offsets, substitutional doping, and schottky barriers of bulk and monolayer inse, Phys. Rev. Mater. **1**, 044004 (2017).

[123] G. Wang, A. Chernikov, M. M. Glazov, T. F. Heinz, X. Marie, T. Amand, and B. Urbaszek, Colloquium: Excitons in atomically thin transition metal dichalcogenides, Rev. Mod. Phys. **90**, 021001 (2018).

[124] M. E. CASIDA, Time-dependent density functional response theory for molecules, in *Recent Advances in Density Functional Methods*, pp. 155–192.

[125] T. Sander, E. Maggio, and G. Kresse, Beyond the tamm-dancoff approximation for extended systems using exact diagonalization, Phys. Rev. B **92**, 045209 (2015).

[126] T. Sander and G. Kresse, Macroscopic dielectric function within time-dependent density functional theory—Real time evolution versus the Casida approach, The Journal of Chemical Physics **146**, 064110 (2017).

[127] C. Tarrio and S. E. Schnatterly, Interband transitions, plasmons, and dispersion in hexagonal boron nitride, Phys. Rev. B **40**, 7852 (1989).

[128] X. Wang, W. Meng, and Y. Yan, Electronic band structures and excitonic properties of delafossites: A gw-bse study, Journal of Applied Physics **122**, 085104 (2017), https://pubs.aip.org/aip/jap/article-pdf/doi/10.1063/1.4991913/15201223/085104_1_online.pdf.

[129] D. Kaplan, Y. Gong, K. Mills, V. Swaminathan, P. M. Ajayan, S. Shirodkar, and E. Kaxiras, Excitation intensity dependence of photoluminescence from monolayers of mos2 and ws2/mos2 heterostructures, 2D Materials **3**, 015005 (2016).

[130] E. Torun, H. P. C. Miranda, A. Molina-Sánchez, and L. Wirtz, Interlayer and intralayer excitons in mos_2/ws_2 and $mose_2/wse_2$ heterobilayers, Phys. Rev. B **97**, 245427 (2018).

[131] C. Cardoso, D. Soriano, N. A. García-Martínez, and J. Fernández-Rossier, Van der waals spin valves, Phys. Rev. Lett. **121**, 067701 (2018).

[132] Y. Li, B. Yang, S. Xu, B. Huang, and W. Duan, Emergent phenomena in magnetic two-dimensional materials and van der waals heterostructures, ACS Applied Electronic Materials **4**, 3278 (2022), https://doi.org/10.1021/acsaelm.2c00419.

[133] A. Ghosh, S. Jana, M. Hossain, D. Rani, S. Smiga, and P. Samal, Structure files are available, https://doi.org/10.5281/zenodo.15488253.